UNIVERSITÀ
DEGLI STUDI
DI PADOVA

Sede Amministrativa: Università degli Studi di Padova

Dipartimento di Fisica e Astronomia "G. Galilei" CORSO DI
DOTTORATO DI RICERCA IN FISICA CICLO XXIX

How Turbulence affects living systems? From micro to macro-scales.

Coordinatore: Ch.mo Prof. Dall'Agata

Supervisore: Ch.mo Prof. Amos Maritan

Dottorando Milo Abolaffio

Ai miei nonni, esempio di vita.

Acknowledgements

Amos Maritan, è un maestro che rammarico di non aver potuto frequentare abbastanza per cause di forza maggiore; non potrò mai smettere di ringraziarlo per la sua gentilezza, la libertà che mi ha consesso e i suoi preziosi consigli e insegnamenti. Insieme a lui ringrazio tutti i membri del LIPh lab che mi hanno accompagnato in questo percorso, in particolare Samir Suweis, Jordi Hidalgo e Jacopo Grilli per tutto l'aiuto che mi hanno dato, e poi Daniel Maria Busiello, Rodrigo Rocha, Loren Kocillari, Chengyi Tu. Matteo Adorisio tra tutti merita una speciale mensione per la sua calorosa e generosa amicizia. Tra i miei compagni di dottorato non posso non ringraziare Giulio Vandin, sia per le tante fruttuose discussioni sulla fisica sia per essere riuscito a distrarmi da essa nei momenti giusti, Alecce Antonio, Moschini Laura, Hierro Ignacio "Nachos", Valerio Volpati e Boso Alberto. Sono veramente grato a tutte le persone con cui ho avuto modo di collaborare: Stefano Focardi, che mi ha insegnato tanto oltre l'ecologia e la statistica e il cui entusiasmo e la passione per i dettagli mi hanno trasportato negli ultimi mesi del dottorato; Antonio Celani, il cui rigore scientifico e profondità di pensiero rimangono un obbiettivo da raggiungere; l'instancabile e entusiasta coppia, innamorata della ricerca, formata da Jacopo Cecere e Simona Imperio (seguiti da il piccolo Edo ovviamente!) e non da ultimo tutti i collaboratori di Stefano (Sonia Lombardi, Andy Reynolds e Massimo Materassi) per gli splendidi momenti di scienza e diletto passati insieme. Michele Salvestroni e Pietro Lenarda sono stati dei preziosi alleati nel mio tour attraverso le simulazioni con ele-

menti finiti. Molte persone non sono state direttamente coinvolte nella mia attività di ricerca ma hanno contribuito a renderla possibile e divertente. Voglio ringraziare per questo i miei genitori, mio fratello e i miei nonni, che hanno sempre creduto in me, e tutti i miei amici. Tra questi Eleonora Lallo, Mika Straka, Beatrice Berti e Sara Filippi, che mi hanno incoraggiato nei momenti più bui, Giulia Lanzirotti e Rachele Dami che mi hanno sensibilizzato alla bellezza della lingua inglese e alle sue difficoltà e Laura Cattozzo, piccolo grande esempio di forza di volontà.

Abstract

In this thesis, we study from a physics perspective three problems related to how turbulence affects living systems. The first problem is an aim to quantify how turbulence changes the uptake of nutrients of micro-organisms, using analytical and numerical simulations. The second problem is a quantification of the relationship between the marine turbulence level depicted as the mixed layer depth and the distribution of foraging points of pelagic birds while the third problem is a verification of the theory of olfactory cued navigation in pelagic birds. In the latter we used calculation from turbulence theory and statistical analysis of real GPS tracks.

0.1 A turbulent introduction

Turbulence is ubiquitous in nature, from far galaxies to the milk stirred by the spun in our morning cup. Natural turbulent flows are highly chaotic and irregular on the small scales, but often characterized by coherent structures on large scales and both of them that can deeply influence underlying dynamics. The exemplary case is the ocean, where the great currents are responsible for general oceanic circulation while the turbulent mixing in the upper layer of the sea, called the mixed layer is crucial for micro-organism life. Ecologically, both scales are deeply related as in the majestic phenomena of plankton blooms. These are initialized by the change in depth of the mixed layer during spring times, which enhances the growth of planktonic organisms, which finally are advected by the oceanic currents over thousands of kilometers. Furthermore, turbulence enhances the rate of encounters among micro-organisms, an important factor both for reproduction and for predation, and increases the nutrient uptake of algae and bacteria. In the process of stirring and mixing, substances dissolved in turbulent waters are on the one hand homogenized on the large scale but, on the other, form fractal structures on small scales. Quantifying the impact on nutrient uptake due turbulence in micro-organisms is still an open question, given the many temporal and spatial scales involved. The intensity of turbulence in the upper layer of the sea, and so its depth penetration, can strongly influence the marine ecology, since beside the already mentioned importance for phytoplankton survival, it can influence the distribution and survival of eggs of pelagic fishes and all other microorganisms. On even a greater scale, the different species that inhabit the sea produce unique odour bouquets that can be learnt and associated to the respective macro-areas. These odour bouquets evaporate from the oceans and are transported by the wind far away from the source and stirred and dispersed by the wind associated turbulence. In the visibly featureless ocean, this irregular and stochastic signal can be

used by birds for navigation that, otherwise, in long trips would become impracticable.

0.2 Topics of the thesis

This thesis studies how turbulence affects living systems. As far as turbulence has many scales, it affects all living creatures, from micro-organisms to big animals in many ways: increasing the amount of nutrient uptakes, shaping the nutrient rich areas in the sea, and transporting precious information over the sea. Therefore, after a short fluid dynamic introduction in section 1, we will move to study how turbulence changes the uptake of nutrients by micro-organism in section 2. This study was motivated by some recent articles that brought evidences that E. Coli has an enhanced growth rate in turbulence beyond the theoretical expected values. Section 2 is therefore devoted to the study of how turbulence affects the nutrient uptake of E. Coli, by means of numerical simulations and analytical calculations. We will provide stronger evidences that the growth rates depicted in the experiments can not be explained with the turbulence levels reported in the latter. In section 2, we also present a study on the role of temporal correlation in fluid flow in nutrient uptake of small organisms. In section 3, we change subject and we study the distribution of foraging points of pelagic birds, specifically shearwaters, with respect to the depth of mixed layer and other candidate variables. Finally in section 4, we will relate the pdf of unidirectional flights in shearwaters and atmospheric turbulence depicted as the mean wind, providing strong evidences of odour-cued navigation in shearwaters.

Contents

Chapter 1

Essentials of fluid dynamics

> There is a physical problem that is common to many fields, that is very old, and that has not been solved. It is not the problem of finding new fundamental particles, but something left over from a long time ago, over a hundred years. Nobody in physics has really been able to analyze it mathematically satisfactorily in spite of its importance to the sister sciences. It is the analysis of circulating or turbulent fluids.
>
> Feynmann, The Feynman Lectures on Physics Vol 1

The dynamics of sea waves, the bathtub vortex as water drains from the home wash basin, or the complicated motion pattern of the honey dripping from a spoon on a slice of cheese, can be all described by the same equation, namely the Navier-Stokes equation, that for an incompressible fluid flow e.g.

a fluid flow for which

$$\nabla \cdot \mathbf{u} = 0 \tag{1.1}$$

can be written as

$$\rho \left(\frac{\partial \mathbf{u}}{\partial t} + \mathbf{u} \cdot \nabla \mathbf{u} \right) = -\nabla p + \mu \nabla^2 \mathbf{u} + \rho \mathbf{g} \tag{1.2}$$

where

- ρ is the density (SI units: $\mathrm{kg/m^3}$),
- $\mathbf{u}$ is the flow velocity,
- ∇ is the divergence,
- μ is the dynamic viscosity (SI units: Pa·s),
- p is the pressure,
- t is the time,
- $\mathbf{g}$ represents external body acceleration like gravity, inertial accelerations and so on.

It is worth noting that the Navier-Stokes equations, although well known for more than a century, are still an active and prolific field of research since the macroscopic phenomena associated with them can be extremely complex and articulated. The great variety of phenomena, emerging from the same equations, is associated with the non-linearity which is present in the governing equations (although also the boundary conditions at the fluid interface can be non-linear). One of the most fascinating phenomena of fluid dynamics is the so-called transition to turbulence, of which the best-known example is still the original experiment, made by Reynolds, of a fluid flow through a circular tube. Reynolds showed that, as the flow rate is increased beyond some critical value, the flow passes from a time-independent one-dimensional flow, called *laminar*, to a time-dependent and fully three-dimensional flow, called

turbulent. Reynolds showed that an adimensional number called Reynolds number, *Re*, can describe this transition. The Reynolds number weights the importance of the destabilizing non-linear advective term and the smoothing Laplacian term in equation 1.2, and it is defined as:

$$\mathrm{Re} = \frac{\rho u L}{\mu} = \frac{u L}{\nu} \tag{1.3}$$

where:

- u is a characteristic magnitude of velocity (m/s),
- L is a characteristic linear dimension (m),
- ν is the kinematic viscosity of the fluid (m^2/s),
- μ is the dynamic viscosity (SI units: Pa·s).

Now we can have a better definition of laminar and turbulent flow: laminar flow occurs at low Reynolds numbers, so when the viscous forces are dominant and is therefore characterized by smooth and constant fluid motion; instead, turbulent flow is characterized by chaotic eddies and unpredictability and occurs at high Reynolds numbers, namely when the inertial non-linear forces are dominant. For very high Reynolds numbers, however, we can recover a predictability in a statistical sense: the statistics of the velocity field in a certain range of scales becomes universal and the flow is characterized by scale invariance. These properties are an effect of the tendency of large eddies to disrupt into smaller eddies and so forth, a process that is well described by a poem of 1921 by Lewis Fry Richardson:

> Big whirls have little whirls
> Which feed on their velocity;
> And little whirls have lesser whirls,
> And so on to viscosity
> in the molecular sense.

The idea of a scale invariance in turbulence was firstly formalized in 1941 by Kolmogorov in a series of articles, in which he presented a theory that we will shortly describe in subsection 1.3. In the following, we will choose a more quantitative approach, adimensionalizing the NS equations and looking at their behaviour in the two opposite limits of high and low Reynolds numbers.

1.1 Adimensionalisation of NS equations

In order to simplify the equation, it is common to introduce a modified pressure that effectively combines the effects of nominal pressure and the external field term $\mathbf{g}$ when the latter is a conservative field. Therefore, if $\mathbf{g} = -\nabla\phi$, we can define a new pressure term $p = p + \phi$, reducing the Navier-Stokes equations to

$$\rho\left(\frac{\partial \mathbf{u}}{\partial t} + \mathbf{u}\cdot\nabla\mathbf{u}\right) = -\nabla p + \mu\,\nabla^2\mathbf{u} \tag{1.4a}$$

$$\nabla\cdot\mathbf{u} = 0. \tag{1.4b}$$

In order to adimensionalize equations 1.4, we have to specify at least three independent dimensional parameters: a characteristic length scale, l_c; a characteristic velocity scale, U_c; and a characteristic time scale T_c. The length scale is usually evident from the geometry of the flow domain; for example, for a sphere moving in an unbounded domain the sphere radius is taken, while the characteristic velocity scale U_c represents a typical magnitude of fluid velocities in the flow. The choice of T_c depends on the boundary conditions: if the boundary conditions are steady, the natural choice for T_c is l_c/U_c, namely the time that a fluid element employs to travel a distance l_c, while if either the boundaries are not static or the flow at large distances is time-dependent, we have to choose another time scale. If the boundary conditions are periodic, then T_c is proportional to the inverse of the frequency, while in other cases the definition of T_c is not straightforward. For the pressure scale, it exists more than a natural choice: for high Reynolds numbers

is usually taken $p^* = \frac{p}{\rho U^2}$ and for low Reynolds numbers $p^* = \frac{pL}{\mu U}$. For high Reynolds numbers, by substituting the scales, using the correct one for the pressure, the non-dimensionalized equation obtained is

$$\frac{1}{St}\frac{\partial \mathbf{u}}{\partial t} + (\mathbf{u}\cdot\nabla)\mathbf{u} \ = -\nabla p + \frac{1}{Re}\nabla^2\mathbf{u}. \tag{1.5}$$

We can clearly see that, for high Reynolds numbers, the viscous term is subdominant, although can not be neglected, since the limit $\nu = 0$ is a singular limit [1]. Instead, in case of low Reynolds numbers the equation becomes:

$$Re\left(\frac{1}{St}\frac{\partial \mathbf{u}}{\partial t} + (\mathbf{u}\cdot\nabla)\mathbf{u}\right) \ = -\nabla p + \nabla^2\mathbf{u}. \tag{1.6}$$

For very low Reynolds numbers and $St \sim \mathcal{O}(1)$, we can neglect the inertial and the time derivative terms, obtaining the Stoke equation:

$$\nabla^2\mathbf{u} - \nabla p = 0. \tag{1.7}$$

We will now treat separately the two limits.

1.2 Low Reynolds number

In order to obtain the Stokes-equations, also called the creeping-flow equations, we have to satisfy both the conditions $Re \ll 1$ and $Re/St \ll 1$, or just $Re \ll 1$ when the boundary conditions are steady. When these conditions are satisfied, the time derivative in the equations of motion can be neglected. Therefore, even if a time dependence can still be present in the problem, as it happens when boundary conditions are changing over time, time is rather a parameter than a variable. In fact, the flow field adjusts instantaneously with respect to the time scale of the boundary conditions, being so always in the steady state with respect to the respective boundary conditions. For this reason, creeping flows are also called quasi-steady flows.

1.2.1 Swimming at low Reynolds Numbers

Bacteria like E. Coli has a typical velocity of 20 μm/s and a dimension of 2μm. The Reynolds number for a swimming E.Coli in water at 20° where[1] $\nu \sim 10^{-6}$ m^2/s, is 4×10^{-5} and allows us to use the Stokes equation to describe the fluid flows in its surroundings. Equations 1.7 are linear and time-independent. It follows that, in order to move itself, a swimming micro-organism has to perform cyclic non-reciprocal motion. The so-called scallop theorem [2] summarizes the precedent statement: a scallop is known to have only one degree of freedom in configuration space and is allowed to perform only reciprocal motion, namely open or close its shell. If we minimize the scallop into the bacterial microscopic world, it would only be able to wobble back and forth around its initial position. Therefore, in order to swim at low Reynolds numbers, microorganisms have developed peculiar ways of motion, for example, by means of helical flagella or flexible oars. It is a common experience that if we suddenly stop swimming while doing it, we still advance of a significant portion of our body. It is interesting to see what happens in the microscopic world of bacteria if they perform the same operation. Let us start with the $f_{drag} \sim \eta u l$, the coasted distance is so $d \sim u^2/a = m_{bac}u^2/f_{drag} = m_{bac}u/\eta l$ where m_{bac} is the bacterial mass. Expressing m_{bac} as $\rho_{bac}l^3$ we find that $d/l = Re\rho_{bac}/\rho$, that for the typical values of an E.Coli brings to $d \sim 0.1$ nm. We can see that for small Re, the Reynolds number can be interpreted as the coasting distance expressed in body length unity. Once again, we showed that inertial forces at low Reynolds numbers are neglectable. As a direct consequence, Newton's law can be replaced by an instantaneous balance between external and fluid forces and external and fluid torques:

$$\boldsymbol{F}_{ext} + \boldsymbol{F}_{int} = 0 \quad \boldsymbol{L}_{ext} + \boldsymbol{L}_{int} = 0. \tag{1.8}$$

[1] see appendix for a table of kinematic viscosity at various temperatures

The hydrodynamic force F and torque L, acting on the body immersed in a fluid flow, are found by integrating the stress tensor $\boldsymbol{\sigma} = -p\mathbf{1} + \eta(2\boldsymbol{E})$, where $\mathbf{1}$ is the identity tensor, over the body surface S, namely

$$F = \int_S \boldsymbol{\sigma} \cdot \boldsymbol{n} dS, \qquad L = \int_S \boldsymbol{x} \times (\boldsymbol{\sigma} \cdot .\boldsymbol{n}) dS. \tag{1.9}$$

$\boldsymbol{x}$ is the position on the surface with respect to an arbitrary origin o and $\boldsymbol{n}$ is the normal to the surface pointing into the fluid. The linearity of the stokes equation forces a linear relationship between the couple velocity $\boldsymbol{u_b}$ and rotation rate $\boldsymbol{\omega_b}$, and the couple external force and external torque, namely

$$\begin{pmatrix} \boldsymbol{F} \\ \boldsymbol{L} \end{pmatrix} = \begin{pmatrix} \boldsymbol{A} & \boldsymbol{B_o} \\ \boldsymbol{B_o^T} & \boldsymbol{C_o} \end{pmatrix} \begin{pmatrix} \boldsymbol{u_b} \\ \boldsymbol{\omega_b} \end{pmatrix}. \tag{1.10}$$

The matrix in 1.10 is called the resistance matrix of the body, and its inverse matrix is called the mobility matrix. The matrices $\boldsymbol{B_o}$, $\boldsymbol{B_o^T}$ and $\boldsymbol{C_o}$ depend on the arbitrary point o chosen as origin of the reference system. However there exists a unique point, $\boldsymbol{p}$, inside the particle where $\boldsymbol{B_p} = \boldsymbol{B_p^T}$. This point is called the centre of reactions of the particle. For highly symmetric bodies, like a sphere, in the centre of reaction $\boldsymbol{B_p} = 0$, and $\boldsymbol{p}$ is called the hydrodynamic point of the particle. For this kind of bodies, translational motion and rotation are disentangled. This obviously is not the case of chiral bodies as the helical flagella of E.Coli where there is a coupling between angular motion and trust.

1.2.2 Analytical solutions

Although the Stokes equations are linear, their solution even for simple geometries can be a difficult task. Like in electromagnetism, an approximation with the first few terms of the multipoles decomposition of the flow field is adopted. This description can be sufficient to describe the flow field only far away from the bacteria itself, although it succeeds in describing the circular motion of E. Coli near a surface [3]. In the following, instead, we will be

interested in the complete analytical solution of the Stokes equation. The solutions for a still sphere in a uniform flow or in a general linear flow, are one of the few known (reported in the appendix). The solutions for an ellipsoid in the same kind of flows are known but difficult to handle, both numerically and analytically [4], while for more general geometries numerical methods are mandatory, for which we refer to chapter 2.

1.3 High reynolds number

> Doue la turbolenza dellacqua rigenera, doue la turbolenza dellacqua simantiene plugho, doue la turbolenza dellacqua siposa
>
> Leonarda da Vinci, Codice Atlantico

In his 1941 paper, Kolmogorov argued that, in the chaotic energy transfer through scales, the directional biases present in large scales are lost along with all the information about the eddies geometry. It follows that eddies down a certain scale become homogeneous and isotropic. This fact was summarized by Kolmogorov in his first similarity hypothesis:
At sufficiently high Reynolds numbers,the local average properties of the small-scale components of any turbulent flow are statistically isotropic and determined entirely by kinematic viscosity ν and the average rate of dissipation per unit mass ϵ.

Therefore the statistics of small-scale motions are universal in every high Reynolds number turbulent flow, independently from the mean flow field and the boundary conditions. From this hypothesis, it is easy to find the so-called Kolmogorov microscales namely the smallest scales present in the turbulent flow, where viscosity dominates and the turbulent kinetic energy is dissipated into heat: As we saw in eq. 1.5 for high Reynolds numbers there

Kolmogorov length scale	$\eta = \left(\frac{\nu^3}{\epsilon}\right)^{1/4}$
Kolmogorov velocity scale	$u_\eta = (\nu\epsilon)^{1/4}$
Kolmogorov time scale	$\tau_\eta = \left(\frac{\nu}{\epsilon}\right)^{1/2}$

exists a whole range of scales where dissipation is negligible. Kolmogorov formulated [5] this concept in his *second similarity hypothesis* that states: *In every turbulent flow at sufficiently high Reynolds number, there is an upper subrange called inertial subrange in which the local average properties are determined only by the rate of dissipation per unit mass ϵ (then being independent on ν).*

The given definition of the Reynolds number allows us to define a Reynold number associated with every scale $Re(l) = u(l)l/\nu$. The Reynolds number at the Kolmogorov length scale $Re(\eta)$ is equal to 1, consistently with the hypothesis that the cascade proceeds until a scale where dissipation balances the non-linearities present in the NS equation. For $l \ll \eta$, as for small bacteria in normal marine flows, $Re(l) \ll 1$ implying that the flux is dominated by dissipation and the flow field is smooth, although still time-dependent and chaotic. A representative scheme of the energy spectrum for stationary turbulence is depicted in figure 1.1: the kinetic energy is injected at the integral length scales, namely the largest scales in the energy spectrum containing the greatest amount of energy, and is transferred towards lower scales in the inertial cascade until it reaches the dissipation range where it is transformed into heat.

1.4 The gradient matrix

We will see that of great interest is the gradient matrix $A = \nabla u$. The matrix A is usually divided into its symmetric and anti-symmetric parts, namely the strain rate tensor $E = \frac{A+A^T}{2}$ and the rate of rotation tensor $\Omega = \frac{A-A^T}{2}$.

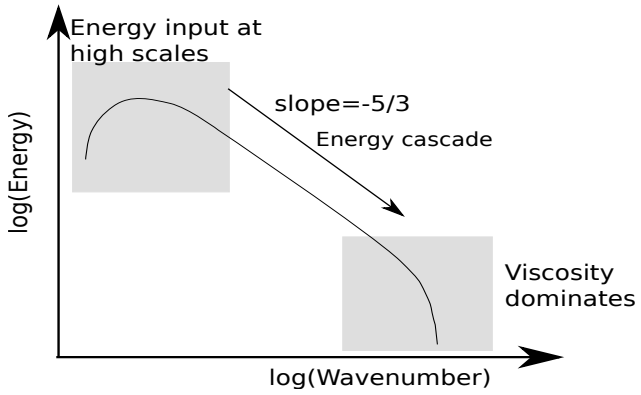

Figure 1.1: An illustrative scheme of the energy spectrum in turbulence.

For incompressible fluids, E is traceless and represents a gradual shearing deformation, with no change in volume. The vorticity vector ω, that offers a more immediate representation of the rotation, can be easily obtained by the rate of rotation tensor:

$$\omega = 2(\Omega_{32}\boldsymbol{e_1} + \Omega_{13}\boldsymbol{e_2} + \Omega_{21}\boldsymbol{e_3}).$$

1.4.1 Statistics of the gradient matrix in turbulence

In turbulence the dissipation rate $\epsilon = 2\nu E_{ij}E_{ij}$ displays large levels of intermittency, nearly log-normal[2] statistics.

Similar trends hold for the pseudodissipation, $\epsilon' = 2\nu A_{ij}A_{ij}$, whose statistics is even closer to log-normality than ϵ.

The variance of the logarithm of dissipation is known to increase with Reynolds number [6] and can be parametrized following Kolmogorov [7] as: $\sigma^2_{\ln\epsilon} = A + (3\mu/2)\ln(R_\lambda)$. A depends on large-scale motions of length L and for isotropic turbulence has been estimated as $A = -0.863$, while μ is an intermittency exponent estimated as $\mu = 0.25$ and $R_\lambda = (L/\eta)^{2/3}$. Obviously the mean of the dissipation should be the mean dissipation rate, and there-

[2] we remind that the pdf of a log-normal is $f(x) = \frac{e^{-\frac{(\ln x-\mu)^2}{2\sigma^2}}}{x\sqrt{2\pi}\sigma},\ x > 0.$

fore, in stationary turbulence, the amount of energy injected per unit time at large scales .

1.5 Scalar transport

Of primary interest in physics, engineer and biology it is the problem of a scalar, for example nutrients, ink, odours or even temperature when temperature differences are not enough to produce significant density gradients, advected by a fluid flow. This problem is well described by the advection-diffusion equation,

$$\frac{\partial C}{\partial t} = -\boldsymbol{u}\boldsymbol{\nabla} C + D\nabla^2 C, \tag{1.11}$$

where C is the scalar concentration and D the molecular diffusivity. As for the Navier-Stokes equation, as we will see in chapter 2, analytical solutions of eq 1.11 are difficult to obtain even for simple geometries and boundary conditions. The two terms in eq. 1.11 have opposite effects: while the advective term tends to stretch, fold and stir the scalar, the diffusive term tends to homogenize and smooth the concentration field. The Peclet number Pe is an adimensional number, defined as the ratio of the advective transport rate to the diffusive transport rate:

$$Pe = \frac{l_c u_c}{D}. \tag{1.12}$$

In general, for low Pe the concentration field is smooth, while for high Peclet the concentration field becomes more and more stirred reaching a fractal distribution [8] in case of chaotic flows and high Pe numbers. In turbulence there is a cascade of the scalar concentration similar to the one of turbulent kinetic energy, where the scalar concentration is transported to smaller and smaller scales until the scalar molecular diffusivity dominates [9]. As done for the turbulent energy we can define the scalar micro-scale, namely the Batchelor microscale (λ_B), that describes the smallest length scales of

fluctuations in scalar concentration before they are smoothed by molecular diffusion, defined as:

$$\lambda_B = \left(\frac{\eta}{Sc^{1/2}}\right) = \left(\frac{\nu D^2}{\epsilon}\right)^{\frac{1}{4}} \tag{1.13}$$

where Sc is the Schmidt number, namely the ratio respectively momentum and mass diffusivity: ν/D. For $Sc > 1$ the Batchelor scale is smaller than the Kolmogorov micro-scales and therefore the scalar have structures smaller than the smallest eddy size.

Chapter 2

Micro-scale

Sea micro-organisms are the basis of the food chain and they have an extreme importance in carbon cycle [10]. Sea waters are poor of food, making the uptake of nutrients the bottleneck in their growth rate. Recent experiments [11, 12] have shown an increased growth rate, and therefore an increased uptake of nutrients, of *E. Coli* in turbulent flows far beyond the expected theoretical value which has brought many authors to consider these experiments as flawed [13]. However, no one has yet proposed clear evidences of what the flaws of the experiments were, leaving the question of their validity still open. The effect of turbulence on the uptake of micro-organisms is not trivial. At large scales it mixes both the nutrients and the micro-organisms population[1], it reduces chemotaxis [15], by "disorientating" the micro-organisms while "rotating" them, and at micro-scales it enhances the nutrients uptake. The linear dimension of micro-organisms, like bacteria and algae (E. Coli typical dimension $\sim 2\mu m$ [16]), in ordinary natural flow field (e.g. marine or lake turbulence), are usually far smaller than the Kolmogorov scale η (typical value ranging between $0.3mm$ and $2mm$ [17]) and therefore than all the length-scales of the turbulent flow. Micro-organisms can be denser than the surrounding water, but their inertia is not enough to

[1] although on the other side, it can clusterize them, see [14]

avoid them to follow the flow lines. This can be seen by comparing two time scales, the Kolmogorov time scale and the Stokes time,

$$\tau_p = \frac{a^2}{3\nu\beta}$$

where a is the linear dimension of the micro-organism and β is the density contrast:

$$\beta = \frac{3\rho_f}{\rho_f + 2\rho_p}$$

where ρ_f is the fluid density and ρ_p is the micro-organism density. Their ratio, τ_p/τ_η, is called the Stokes number and it quantifies the departure of inertial particles, which in our case are the micro-organisms, from fluid particles trajectories. Using a density of $1.1\rho_f$, as normally found for E. Coli [16], and common values of turbulence levels and a dimension of 1 μm, we obtain a Stokes number lower than 10^{-3}, indicative that departures of non-motile micro-organism trajectories from fluid particle trajectories are negligible [18, 19]. Therefore, in the reference system of a non-motile bacteria, the undisturbed flow field, namely the flow field without the presence of the micro-organism, can be approximated in its surroundings with the first term in the Taylor's series expansion,

$$U_\infty(\boldsymbol{X}) = +A\boldsymbol{X} + K : \boldsymbol{X}\boldsymbol{X} + ...+ \sim A\boldsymbol{X}, \tag{2.1}$$

where $\boldsymbol{X} = 0$ is the hydrodynamic center of the organism and the matrix A is the gradient matrix introduced in paragraph 1.4. A field that can be expressed as $\sim A\boldsymbol{X}$ is called a linear flow. As mentioned in section 1.2.1, the Reynold number at the bacteria scale is far below 1, and the fluid flow surrounding the micro-organism, obeys the Stokes's equation for incompressible fluids, matching at first order the linear flow $A\boldsymbol{X}$ of equation 2.1 far from the micro-organism and no sleep boundary condition on the micro-organism surface. The solution for this problem in the case of a sphere is reported in appendix B.1.1. In turbulence the boundary conditions at

infinity, namely the matrix A, are time dependent, e.g. $A = A(t)$, but as mentioned in section 1.2, since $St \sim 1$ in turbulence, time is rather a parameter than a variable and the flow field is considered quasi-steady in the definition we gave in section 1.2. In order to obtain the uptake of a micro-organism, we have to solve the advection-diffusion equation 1.11. In order to simplify the problem, we will suppose, as boundary conditions, total absorption on the micro-organism's surface and a constant concentration far away from the micro-organism, namely:

$$C(\boldsymbol{x} \in S) = 0, \qquad \lim_{||\boldsymbol{x}|| \to \infty} C(\boldsymbol{x}) = C_\infty \tag{2.2}$$

where S is the micro-organism's surface and $\boldsymbol{x} = 0$ is its hydrodynamic center (or the center of reaction if the latter does not exist). Once solved the time dependent equation 1.11 with boundary conditions as in equations 2.2, a time dependent matrix $A(t)$ and an initial concentration field C_0, the instantaneous uptake of nutrients, due to the no sleep boundary condition of the flow, imposed on the organism surface, is simply

$$F(t) = D_0 \int_S \boldsymbol{n} \cdot \boldsymbol{\nabla} C(t) dS. \tag{2.3}$$

The change in the uptake of a micro-organism, by virtue of the fluid flow, is quantified by the Sherwood number, Sh , which is analogous to the Nusselt number for heat-fluid dynamics. The Sherwood number is defined as the ratio of the advective nutrient uptake and the diffusive nutrient uptake. Numerous works relate the Sherwood number to the Peclet number, Pe, namely the ratio of the advective transport rate to the diffusive transport rate. For a spherical particle in a stationary linear flow, Pe is defined, using Einstein convention, as $\sqrt{E_{ij}E_{ij}}r^2/D$, where the matrix E is the symmetric part of the matrix A in eq 2.1, e.g. $E = (A + A^T)/2$ where the capital T stands for transpose. In this configuration, there are analytical results for the Sherwood number in the cases $Pe \ll 1$ with $Sh \sim 1 + 0.36Pe^{1/2}$ [20, 21] and $Pe \gg 1$ with $Sh = 0.9Pe^{1/3}$ [22]. [23] presents a parametrization of

Sh for Pe in range 0.1-90 : $0.82 + 0.63Pe^{0.4}$, obtained thanks to numerical simulations and a fit with a formula $a + bPe^c$. Instead, the anti-symmetric part of A, namely Ω the rotation tensor, can only reduce the uptake since rotation tends to close the streamlines. When $|\Omega|/E < 1$, the difference in the uptake is lower than 10%, while when $|\Omega|/E \gg 1$, counts only E_ω, namely the projection of E on the rotation vector $\boldsymbol{\omega}$. In this last case $Sh = 1 + 0.4\left(r^2|E_\omega|/D\right)$.

In turbulence is used to decompose turbulent flows in mean and fluctuating part, namely $U =< U > +u$. The same procedure can be applied to the strain tensor:

$$E =< E > +e. \tag{2.4}$$

Given that in turbulence flows $<< E_{ij} >< E_{ij} >>\ll << e_{ij}e_{ij} >$, we can suppose valid the following relationship between the shear rate and the kinetic energy dissipation:

$$\epsilon = 2\nu < e_{ij}e_{ij} > . \tag{2.5}$$

Hence, we can introduce the turbulent Peclet number:

$$Pe_{turb} = \frac{r_0^2}{D}\left(\frac{\epsilon}{\nu}\right)^{1/2} = \frac{r_0^2 VRe^{1/2}}{DL}. \tag{2.6}$$

Using the mean E and Ω in an isotropic turbulent flow characterized by a Reynolds number Re, the expected uptake should be[23] for low Pe_{turb}:

$$Sh = 1 + 0.29Pe_{turb}^{1/2}. \tag{2.7}$$

while for high Pe_{turb} it is expected a relationship like $Sh = 0.9Pe^{1/3}$. The sub-linear dependence of Sh on Pe has led some authors [24] to believe that the average nutrient uptake of a micro-organism in a turbulence flow should be lower than the nutrient uptake calculated using Pe_{turb}. In particular [24] calculated an expected reduction in the estimated uptake due to the micro-scale turbulence intermittency between 6.26% and 19.07% for small Pe_{turb} and a reduction between 21.22% and 61.78% for high Pe_{turb} using normal values of marine turbulence.

2.1 Case of study

In the two already mentioned articles [11, 12] (from now on we will refer to them as Exp_1 and Exp_2) E. Coli have been put in an "oscillating grid reactor under conditions of no oxygen transfer to the liquid phase." "The reactor consisted of a Plexiglas chamber with dimensions $50 \times 50 \times 47$ cm and a vertically oscillating grid made from Plexiglas rods $48 \times 1.3 \times 1.3$ cm." "The rods were spaced 5 cm apart. The grid was powered by a rotating motor with a speed controller. The grid was set to oscillate at four frequencies (f=1, 2, 4, and 6 Hz). The stroke length was 3 cm." Measuring the E. Coli concentration at different time intervals, they were able to deduce the growth rate of the bacterial population, where the growth rate of a population is the time constant in the exponential growth phase, and it is related to the doubling time as $T_d = 1/(log_2(e)\mu_g)$ where T_d is the doubling time and μ_g is the growth rate. A summarizing table of their results is presented in table 2.1.

As it is possible to see, the values of Pe_{turb} for the turbulence levels depicted in table 2.1 assuming a characteristic length of 1μm, are very low, and so are the associated theoretical Sherwood numbers. If we assume an equality between the Sherwood numbers and the growth rate, the predicted growth rate should not be greater than 1.044 times the growth rate in still water. Why this discrepancy? Are the experiments flawed? Are the predicted values wrong?

2.1.1 Hypothesis and proposed mechanisms

We want to test the following hypothesis:

Hypothesis *The growth rates presented in experiments Exp_1 and Exp_2 for E. Coli organisms are consequence of an increased uptake due to an isotropic homogeneous turbulence characterized by the parameters presented in table*

Grid frequency	(Hz)	0	1	2	4	6
ϵ	$(m^2/s^3) \times 10^6$	0.0	7.3	29.7	101.0	176.1
μ_g	(1/h)	0.021	0.023	0.059	0.064	0.106
μ_g/μ_{gs}	(-)	1.00	1.13	2.82	3.09	5.10
Re	(-)	0	19	32	86	115
u_{rms}	(mm/s)	0	1.4	2.2	4.9	6.2
v_{rms}	(mm/s)	0	1.4	2.3	4.7	5.9
$\langle \mathbf{v}' \rangle_{rms}$	(mm/s)	0	2.4	3.8	8.3	10.5
τ_η	s	∞	0.37	0.19	0.10	0.075
T	s	(-)	11.9	7.3	10.23	9.39
$Pe_{turb} \times 10^3$	(-)	0	4.7	9.6	17.6	23.3
$Sh(Pe_{turb})\times$	(-)	1.0	1.020	1.028	1.039	1.044

Table 2.1: Re is evaluated at the integral length scale. $\langle \mathbf{v}' \rangle_{rms}$ was calculated by the author from data as $\sqrt{u_{rms}^2 + v_{rms}^2 + (u_{rms} + v_{rms})^2/4}$ since no information on z_{rms} were available. Values under the middle rule, Pe_{turb} and $Sh(Pe_{turb})$, are calculated by us, assuming a characteristic length of 1 μm and using formula 2.7.

2.1.

We proposed 3 different mechanisms for an enhance in the growth rate and tested them separately:

- The particular geometry of E. Coli: E. Coli has a particular form, different from spherical and possesses flagella. In section 2.2, we will investigate the role of the particular E. Coli's body form, the change in its linear dimension while growing, and the possible role of its flagella in its nutrient uptake.

- The role of temporal dynamic in the fluid flow: the known results of the Sherwood number presented before were obtained by the authors

in case of stationary flows, while [24] average stationary quantities, neglecting the complex spatio-temporal structure of turbulence. In section 2.3, we will investigate the role of temporal dynamics in fluid flows, firstly in the simple geometry of a spherical bacteria, by use of simple exemplary flows. We will show that, for temporal dynamics "similar" to the turbulent ones, an enhanced uptake with respect to the expected values, using the mean quantities, is obtained. We then apply the same methodologies in the geometry of E. Coli, obtaining similar results.

- E. Coli are adders: E. Coli divide with the adder principle. This implies that they divide when the integral of the nutrient flux has reached a certain value. Therefore the fluctuations present in the uptake can boost the growth rate of the overall population.

Finally, in section 2.5 we obtain an upper growth limit combining all the factors mentioned before, in order to reject definitively the hypothesis 1.

2.2 The E. Coli geometry

E. Coli body is usually described like a small cocktail sausage [16], of 0.8 μm of radial diameter and variable length, from 2 μm to 10 μm. It possess usually 4-6 flagella of ~ 10 μm of lengths and $\sim$ 20nm of radius disposed in a helical shape with radius $\sim 0.2\mu$m and pitch of $\sim 2.2\mu$m.
The flagella arise at random from the sides of the cell. If the flagella rotate all CCW they form a bundle at one pole of the bacterium that pushes the cell, while if one or more starts to rotate CW these ones detach from the bundle and disorient the E. Coli. This mechanism is the base of the so called run and tumble way of motion of E. Coli, namely the alternation of periods of traveling and periods of disorientations. This strategy is used by E. Coli to perform chemotaxis [16]. As the cell grows, it gets longer and then divides

in the middle, a mechanism that we will define better in section 2.4.
Therefore in next sections we will schematise the E. Coli body as a solid of revolution with plane projection as a stadium and use as radius of the hemispherical cap $R = 0.4\mu$m and variable length h. We call h_1 the length of the cylindrical part in the middle $h_1 = h - 2R$.

2.2.1 E. Coli body

In stagnant waters the flux toward a micro-organism depends on its geometry. In literature is usually reported a version of the Sherwood number defined as

$$Sh_0 = \frac{Ql_c}{SDC_\infty} \tag{2.8}$$

where l_c is a characteristic length that has to be chosen so that the surface area S is equal to $4\pi l_c^2$ [25]. We stress that in literature often other characteristic lengths are used (and sometimes different definitions of Sh_0) complicating the comparison among different results, and requiring extra-care in order to not fall in errors. For a general linear flow with no rotation and low Peclet numbers, it is usually reported in literature the formula:

$$Sh = 1 + \alpha Sh_0 Pe^{1/2} + \alpha^2 Sh_0^2 Pe + O(Pe^{3/2}) \tag{2.9}$$

where Pe is calculated as $Pe = El_c^2/D$, while for high Pe number we did not find reported formulas. In order to investigate the latter, we performed numerical simulations using an axi-symmetric linear fluid flows, namely a flow field that can be written in the appropriate reference system as:

$$\begin{pmatrix} U_x(\infty) \\ U_y(\infty) \\ U_z(\infty) \end{pmatrix} = \begin{pmatrix} -a/2 & 0 & 0 \\ 0 & -a/2 & 0 \\ 0 & 0 & a \end{pmatrix} \begin{pmatrix} x \\ y \\ z \end{pmatrix} \tag{2.10}$$

where a is the parameter that controls the intensity of the flow field and its direction.

2.2.2 Calculation of Sh_0 for an E. Coli

In order to calculate Sh_0, we solved the diffusion equation using as external boundary condition a sphere with radius $R_{ext} = 10^4 R$. The results are reported in figure 2.1a, together with the analytical prediction of Sh_0 for a prolate ellipsoid of semi-axis length R and $h/2$, often used as a proxy for the E. Coli geometry, see appendix B.1.5. As it is possible to see, the Sh_0 of a prolate ellipsoid overestimates the Sh_0 of the stadium of revolution. The shape factors Π defined as $Pi = Q/(DC_\infty)$, for both the stadium of revolution and the ellipsoid are reported in figure 2.1b where is clear that the shape factor of the stadium is bigger than the shape factor of the ellipsoid. This is expected since both surface and the volume of the stadium are bigger than the respectives of the ellipsoid.

2.2.3 The Uptake of E. Coli in stationary flows

We performed numerical simulations varying the flows intensity parameter a. Instead of searching for an exact theory, we simply performed a fit of the results using the formula:

$$Sh = (0.5 + (0.125 + 0.27 Sh_0 c_1 (Pe)^{0.5 c_2}) + c_3 (1/Sh_0)(0.9^3) Pe)^{1/3} \quad (2.11)$$

for every value of h with free parameters c_1, c_2, and c_3. We then fit again the obtained values c_1, c_2, and c_3 against h, obtaining the complicated formula reported in appendix, section B.1.6, that can describe the flux for every value of a and h with a precision lower than 5 in all the range of the considered values. Finally, we used this formula to perform numerical simulation of the growth of a bacteria, in order to calculate how the doubling time changes for different flows intensity and initial length of the bacteria, called Δ, and we assume that the bacteria divides when it reaches a length 2Δ. The results of these calculations are depicted in figure 2.2.

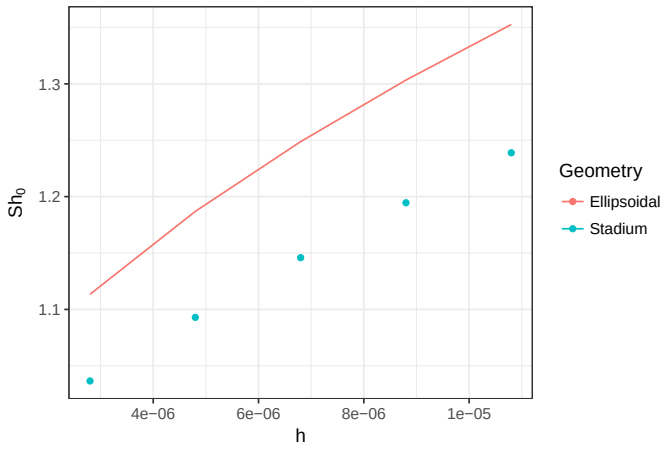

(a) Sh_0 for a stadium of revolution and a prolate ellipsoid with same R and length h. Sh_0 is far greater in the prolate ellipsoid

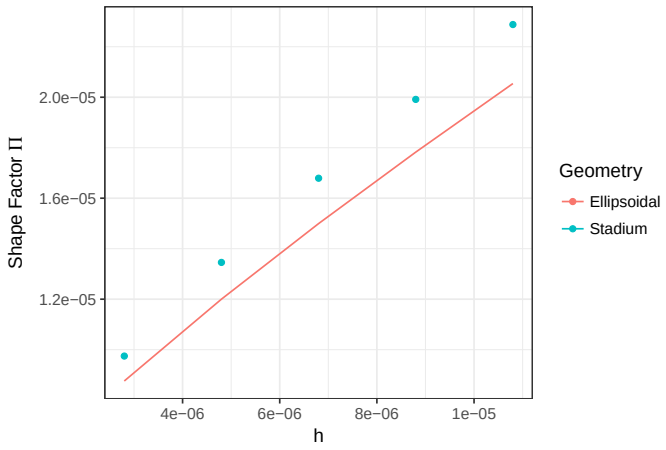

(b) Shape factor for a stadium of revolution and a prolate ellipsoid with same R and length h. The shape factor is bigger for the stadium.

Figure 2.1: Sh_0 and Π for an ellipsoid and a stadium of revolution.

2.2.4 The possible role of E. Coli flagella

The mass of the E. Coli flagella is negligible compared to the mass of its body. However, the hydrodynamic resistance of the E. Coli's flagella to a translational flow directed along its axis is lower but still comparable to the hydrodynamic resistance of its body. In a linear flow the flow intensity scales linearly with the distance. The combination of these two facts implies

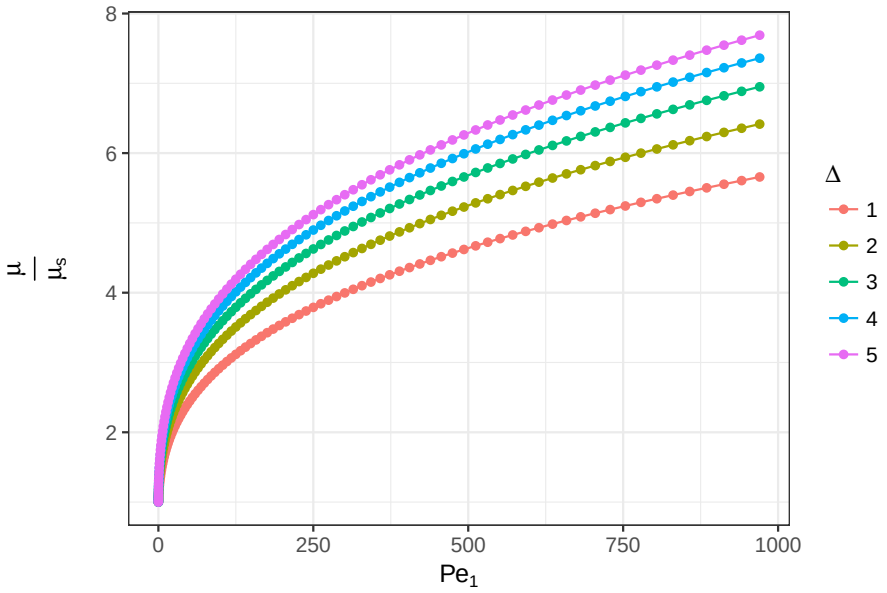

Figure 2.2: Relative growth rate, μ/μ_s for different values of Pe_1 and different values of Δ.

that in a linear axysimmetrical flow, when the E. Coli is directed along the axis of symmetry, the centre of the linear flow cannot be the centre of the bacterial body, but instead should be skewed toward the flagella. The actual difference between the two positions relies on the precise geometries of the E. Coli itself and in particular on the number of present flagella. We will therefore parametrize the position of the linear flow, that can be recast as a linear flow plus a translational flow maintaining the centre of the linear flow in the center of the bacterial body. Naively we might think that the nutrient uptake of the bacteria due to the combination of the two flows, namely the translational and the shear one, is always greater than the the flux due to any of the single ones. Actually, this argument is not true as depicted in [26] where the authors studied the Sherwood number of a sphere in a translational-shear flow at high Pe numbers, finding

$$Sh = k(Pe_{tras} + Pe_{shear})^{1/3} f(Pe_{tras}/Pe_{shear}) \tag{2.12}$$

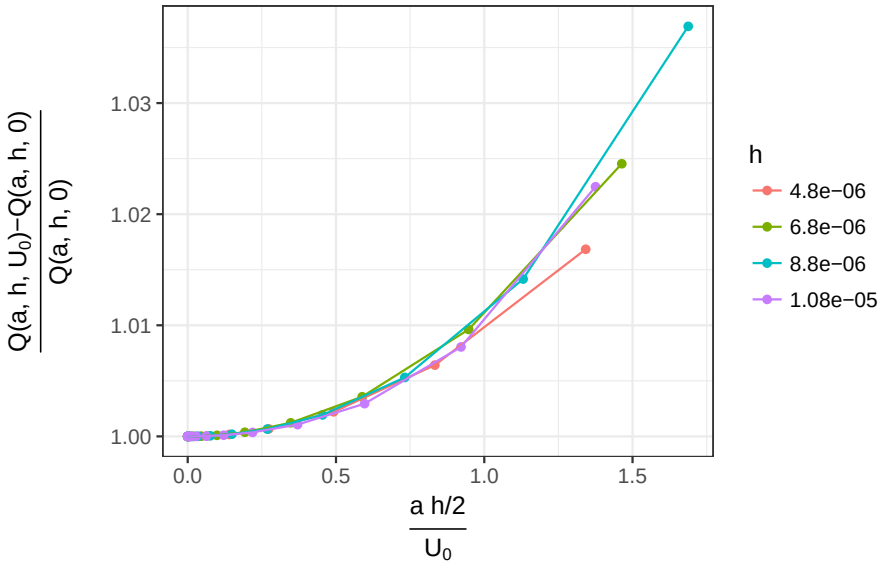

Figure 2.3: Relative difference in the uptake when a translational flow is added to a linear flow.

where k is a constant and f a complicated function involving elliptic integrals of first and second kind, that we will not show, that has a minimum for $Pe_{tras}/Pe_{shear} \sim 1$. We extended the results of [26] performing numerical simulations for the case of a stadium of revolution for various values of h, a and U_{cost}, where the latter is the module of the translational flow added. It is evident that $0 < |U_{cost}| < (h/2 + L/2)a$ where L is the length of the flagella, and the expected value is around $ah/2$. Results are presented in figure 2.3. As it is possible to see, adding a constant flow to a linear flow for a stadium of revolution, brings to a greater uptake than the case of just a linear flow, although the difference is very low, $\lesssim 1\%$, for the range of parameters we are interested: $U_{cost} \sim ah/2$. It is interesting to note that the opposite case of adding a linear flow to a translational flow brings to a decrease in uptake for $U_{cost} \sim ah/2$.

2.3 The role of temporal dynamic on instantaneous nutrient uptake

We will begin with a spherical organism and then pass to an elongated object.

2.3.1 Spherical organism

We will begin showing the results obtained using axi-symmetric flow, e.g. flows that can be described as in eq. 2.10, where now the parameter a, namely the parameter controlling the intensity of the flow field, will be time-dependent, e.g. $a = a(t)$. We will show that time dynamics in fluid flows greatly influences the nutrient uptake of small-organisms. Furthermore, the time dynamics in the fluid flow can produce an enhanced uptake with respect to the stationary case with the same mean Peclet number presented by the former. This conclusion invalidates the arguments of [24], and shows that in every attempt of calculating nutrient uptakes in turbulent flows, corrections due to time dynamics should be taken into account.

In order to demonstrate this, we first analyzed the transient time in the nutrient uptake when a sudden change in the fluid flow occurs. Hence, we considered a fluid flow that passes from $U(a_1)$ to $U(a_2)$ at time $t = 0$, and a concentration field that for $t < 0$ is the stationary solution obtained with a stationary $U = U(a_1)$. Then, we recorded the transient instantaneous uptake $F(t)$. We define F^*, the adimensionsional re-scaled uptake, as

$$F^*(t) = \frac{F(t) - F(a_1)}{F(a_2) - F(a_1)} \tag{2.13}$$

where $F(t)$ is the instantaneous uptake at time t and, $F(a_2)$ and $F(a_1)$ are the stationary uptake for, respectively, $U = U(a_1)$ and $U = U(a_2)$. From the simulations it becomes clear that when the sign of a_1 is equal to the sign of a_2, the transient time depends on the ratio a_1/a_2. If the latter is greater than 1, then the normalized flux, for $t > 1/a_1$, is proportional to $(ta_1)^{0.5}exp(-ta_2)$ while in the opposite case the normalized flux has a exponential dependency

on a_2 with a weak dependency on a_1. As a result the transient time in the case $a_1/a_2 > 1$ is greater than in the case $a_1/a_2 < 1$. Using this argument we were able to construct simple time dynamics were the mean uptake is greater than the uptake obtained with a stationary flux characterized by the same mean Peclet number. For a complete diving into the results we refer the reader to the section in appendix devoted: A However the results presented prove the impossibility of obtaining an instantaneous Sherwood number greater than $Sh(Pe(E_{max}))$ where E_{max} is the maximum value of the shear tensor encountered in the flow history. We checked by mean of full 3-D simulation if this is true for any possible combination of two matrix, verifying that this is true.

2.3.2 Time dynamics for an elongated object

As for the spherical case, we used axi-symmetric flows to the transient time in the uptake for a stadium of revolution. Applying the same procedure depicted previously we change suddenly the linear flow intensity parameter from a_1 to a_2 and looked at the transient time. The elongation has mostly no effect on the transient time, and the results depicted before are still valid. The addiction of a constant velocity has the effect of reducing the transient time when $a_1/a_2 < 1$ while few differences are found for $a_1/a_2 > 1$ implying the possibility of having an even greater uptake due to time dynamics than the expected value obtained using the mean values. However, even for elongated object in general axi-symmetric flows we did not find any possibility of accessing values greater than $F(E_{max}, U_{cost}(E_{max}))$. We will use this result in section 2.5. In section B.1.2 in supplementary, we simulate an ellipsoid in a turbulent flow in order to show that, increasing the eccentricity of the ellipsoid, the correlation time of the projection of the shear tensor on the axis of symmetry increase. This effect can contribute to reduce the depression in uptake due to rotation, but cannot completely

eliminate it, especially in case $|\Omega|/|E| > 1$ when the streamlines far away from the bacteria are closed.

2.4 The adders hypothesis

E. Coli belongs to the class of micro-organism that divides itself according to the adder principle [27], namely a thresholding mechanism in the size added between birth and division, $\Delta = s_d - s_b$, where s_d is the size at division and s_b is the size when the bacteria is born. Δ, although with a certain degree of noise, is constant for a an overall population in a given growth condition [27]. This model implies that for any initial bacterial population size distribution, the asymptotic distribution of new born bacteria lengths will have a mean Δ and the asymptotic distribution of dividing bacteria will have a mean 2Δ. The standard deviation of the distributions of s_b and s_d increases with Δ, while the coefficient of variation is quite constant for all the growth conditions examined by the authors. The basal rate of the bacteria is very low[2], implying that in normal growing conditions most of the nutrient uptake is directly converted into length of the bacteria and therefore in the

[2]The maximal reported value of the basal activity that we found in literature is of $3000W/kg$ (with an actual mean of $300W/kg$). We can have a rough estimate [28] of the basal activity of an E coli $W_b \sim 10^{-14}W$. Using the Stokes law in order to have an estimate of the energy consumption of an E. Coli for traveling we obtain:

$$W_T = 6\pi l\eta u^2 \sim 7.5 \times 10{-}18J/s$$

where we used $l = 8\mu$m in order to have an upper bound. Using the glucose concentration as reported in the experiment Exp_1 ,$C_G = 100mg/L = 10^{-1}Kg/m^3$, the diffusion constant of glucose, $D_G = 5.7\ 10^{-10}m^2/s$, and the glucose energy density, $E_G = 1.5610^7J/Kg$, we can have an estimate of the energetic uptake of a E Coli:

$$W_U = 4\pi l D_G C_G E_G \sim 10^{-8}J/s.$$

where instead we used $l \sim 1$. It's clear to see that although our estimate are very rough there are orders of magnitude between W_U and $W_T + W_b$.

diffusion-limited regime, the division time will depend on the cumulative flux of nutrient to the surface of the E. Coli. In presence of a time dependent fluid flow, the flux fluctuates in time and so does the division time. In case of turbulent flows, fluctuations can be large. We are now questioning if these fluctuations can result in a significant increase in the growth-rate. Assuming random, independently and identically distributed division times we can formalize the process as a renewal[3] process where the events are divisions and the holding times are the intervals between the divisions. Let us consider independent, identically distributed holding times T_n with pdf $f(T)$ and cdf $F(T)$ and let $t_n = \sum_{i=1}^{n} T_i$ be the epoch at which the n-th event occurs. The number of events at time t is

$$N(t) = \sum_{n=1}^{\infty} \mathbf{1}(t_n \leq t) \tag{2.14}$$

where $\mathbf{1}(C)$ is the indicator function, which is 1 if the condition C is true and 0 otherwise. Suppose now that the overall bacterial population of the experiment is divided in bacterial patches that remain together for all the experiment, feeling the same fluxes and therefore replicating all at the same times. If a patch begins with a population B_0, the number of bacteria after a time t is $B_0 2^{N(t)}$. The asymptotic rate of growth ρ of the overall population is

$$\rho \equiv \lim_{t\to\infty} \frac{1}{t} \log_2 E\left[2^{N(t)}\right] \tag{2.15}$$

[3]A renewal process [29] is a generalization of the Poisson process. In essence, the Poisson process is a continuous-time Markov process on the positive integers (usually starting at zero) which has independent identically distributed holding times at each integer i (exponentially distributed) before advancing (with probability 1) to the next integer: $i + 1$. In the same informal spirit, we may define a renewal process to be the same thing, except that the holding times take on a more general distribution. (Note however that the independence and identical distribution (IID) property of the holding times is retained).

For the Jensen's inequality[4]

$$\frac{1}{t}\log_2 E\left[2^{N(t)}\right] \geq \frac{E(N(t))}{t} \tag{2.17}$$

where the equality can hold only if $N(t)$ does not fluctuate. Taking the limit of large times on both sides, it follows that

$$\rho \geq \frac{\log(2)}{E(T)} \tag{2.18}$$

that is, fluctuations in the division times always enhance the growth rate.

A simple example Let us take T to be the first-exit-time at the origin of a constant drift-diffusion process $dX_t = -udt + \sqrt{2D}dW_t$, starting at $X_0 = x$, with $u > 0$. Following calculation expressed in appendix B.1.6, the growth rate is

$$\rho = k(ln2) = \frac{ln(2)}{x/u} + \frac{(ln(2))^2}{x^2/D} \tag{2.19}$$

In equation 2.19 x/u is the ballistic time for absorption and is equal to $E(T)$ while x^2/D is the diffusive time. For $x \lesssim D/u$, the diffusive time is comparable with or shorter than the average time, and fluctuations have a strong effect on the growth rate.

We performed several simulations of the adder mechanism using different solutions to derive the uptake, different geometries and growing mechanisms and different algorithms to simulate the matrix A. None of these trials have produced a growth rate even comparable with the one presented by E_1. Instead of presenting these results, we present in the next section a general rejection of the E_1 results.

[4]Suppose that X is a random variable and ϕ is a convex function, namely a function for which all the line segments between any two points on the graph of the function itself lies above or on the graph, then the famous Jensen's inequality states that:

$$\phi(E[X]) \leq E[\phi(X)] \tag{2.16}$$

2.5 Conclusions

The scope of this section is to find an upper bound in the growth rate in order to definitely reject the hypothesis 1. The growth rate of the population ρ must follow:

$$\rho \leq \frac{1}{t_{min} log_2(e)}$$

where t_{min} is the minimum doubling time of a single bacteria in all the population.

As presented in section 2.3 firstly for a spherical organism and then for an elongated object, if we change the matrix $\boldsymbol{E}$ over time, then $Q(t) \leq Q(E_{max})$, where E_{max} is the maximum value of E in the considered temporal interval. Since t_{min} depends on the nutrient flux, t_{min} is then related with E_{max}, where this time E_{max} is the maximum value of E experimented by all the population between the respective doubling.

In particular, $t_{min} \geq T_d(\Delta, E_{max})$ where $T_d(\Delta, E_{max})$ is the doubling time of a bacteria with Δ and in a linear stationary flow with $E = E_{max}$.

In this line of reasoning we can see the results of section 2.2.3 as $T_d(\Delta, E_{max})$.

The probability that the maximum of a sequence of n independent and identically distributed random variables X_i, with cumulative distribution function F, is under a certain threshold, can be easily derived:

$$\Pr(X_1 \leq z, \ldots, X_n \leq z) = \Pr(X_1 \leq z) \cdots \Pr(X_n \leq z) = (F(z))^n. \quad (2.20)$$

By using now the values present in table 2.1 for the turbulent parameters, and assuming for the matrix E a log-normal distribution parametrized as defined in section 1.4, extended for low Reynolds number as depicted in appendix B.1.4, for E, we can calculate how many uncorrelated gradient matrix #A we have to generate in order to find a E that produces a growth rate as depicted the case of study experiments. The doubling time T_d in still water, in the studied experiments, is $\sim$ 33 h. The smallest time for the gradient matrix A is τ_η, the Kolmogorov time, although it has also a

slow dependence on the integral time. Assuming a decorellation time as τ_η, every bacterium experiments, during an usual doubling time, at most T_d/τ_η uncorrelated gradient matrix during the doubling time. Using the computed values of $T_d(\Delta, E_{max})$, we can find $E_{max}(T_d, \Delta)$ by mean of simple interpolation. Using as T_d the values of the studied experiments, and using as parameter of the E. Coli, $\Delta = 4\mu$m and $R = 0.4$, we obtain the results in table 2.2. In order to express the flow field in an unambiguous way, we express E as the corresponding Pe of sphere of radius 1μm and using the glucose molecular diffusion constant D. We call this measure Pe_1. $Pe_{1\ nec}$ is the same measure, but calculated using E_max, namely $Pe_{1nec} = E_max r^2/D$ with $r = 1mu$m.

Grid frequency	(Hz)	0	1	2	4	6
ϵ	$(m^2/s^3) \times 10^6$	0.0	7.3	29.7	101.0	176.1
μ_g/μ_{gs}	(-)	1.00	1.13	2.82	3.09	5.10
L/η	(-)	(-)	29.1	44.5	70	92.5
τ_η	s	∞	0.37	0.19	0.10	0.075
$T_d/\tau_\eta 10^5$	(-)	∞	2.8	2.2	3.8	3.1
$Pe_{1\ turb} \times 10^3$	(-)	0	4.7	9.6	17.6	23.3
$Pe_{1\ nec}$	(-)	(-)	0.125	34	50	280
$\#A$	(-)	(-)	4 10^4	10^{20}	5 10^{18}	1.5 10^{20}

Table 2.2

The initial concentration of bacteria in the experimental apparatus is 10^6 cells/mL, implying a total amount of $\sim 1.310^11$ bacteria, #B. Between the division times, all the population will experience an overall number[5] of independent gradient matrices $\#B \times T_d/\tau_\eta$. We can clearly see that, for

[5]Since the bacteria number is far way greater than V/η^3 with V the volume of the experiment, and η the smallest scale in the flow, we are over estimating the number of possible independent gradient matrices

all the experiments except the one with low Re, none of the bacteria ever experience a gradient matrix that can barely explain such a great growth rate. It is worth noting that in every passage we used a strictly upper bound, ignoring all the possible mechanisms that will lower the uptake, e.g. rotations, making our statement even stronger. Therefore, we can conclude that, even combining together all the mechanisms proposed in section 2.1.1, the growth rate reported in the experiments Exp_1 and Exp_2, are impossible. We than reject as far as we know the thesis 1.

However, this does not mean that the experiments are necessarily flawed. A careful analysis of the documentation of the experimental apparatus shows that the turbulence is far away from being isotropic [30] and the flow is subject to large scale bistability as reported in [31]. Experiments conducted in similar apparatus [32] showed that: "even in the homogeneous region in the center we see a surprisingly strong dependence on the large scale velocity that remains at all scales. Previous work has shown that similar correlations extend to very high Reynolds numbers." Once again, reporting only the mean quantities could lead to errors and a full record of the flow field should be taken into account. However, if the explanation of such high growth rates is deeply connected with a particular apparatus, a full investigation of the experiment is less interesting since there is a lack of universality in the experiment itself. We have to mention that we ignored the possibility that the E. Coli could be trapped in some regions of high shear flow, or more in general, that the gradient matrix statistics perceived by the E. Coli is different from the gradient matrix statistic of normal fluid particles as presented in literature [14] for flows like cellular or vortical flows. However, recent results [33] concluded that, in case of turbulent flows, the clustering and trapping effects are small if compared to the reported case observed in the simpler flows just mentioned above. Therefore, we can conclude that since the differences between the growth rates recorded in the experiment

and the theoretical expected ones are so big, this last argument can not still explain the enhanced growth rate measured in Exp_1 or in Exp_2.

Chapter 3

From micro to Macro scales

In this chapter, we will analyze how turbulence in the ocean, parametrized by the mixed layer depth, a quantity that we will introduce later on, changes the food resources availability for shearwater birds and therefore their habitat selection.

3.1 The mixed layer

Phytoplankton, in order to grow, needs both light and nutrients. In open sea, these two sources come from different directions: the light comes from the sun and is absorbed by water, decreasing exponentially with depth, while the source of nutrients is at depth. The Euphotic zone is defined as the layer of water in which there is enough light for photo-synthesis to take place, and its depth varies "from only a few centimeters in highly turbid eutrophic lakes, to around 200 meters in the open ocean" [34]. Water currents in ocean are crucial for the ecosystem, since they bring in the euphotic zone the necessary nutrients for life, that otherwise would rapidly become depleted. Since the source of light comes from above, and so the heat, upper waters are warmer than lower waters. However, the temperature profile does not follow a theoretical absorption curve since a strong mixing - due to the

Figure 3.1: A shearwater.

active turbulence generated by different mechanisms like wind, convective cooling, breaking waves, shear flows, and other physical processes - tends to uniform the temperature. As temperature is mixed, so all the other physical parameters - like salinity and density - are mixed. The oceanic mixed layer is then defined as the layer between the ocean surface and a certain depth where a given physical parameter of the ocean state (e.g. temperature, salinity, density) is almost vertically uniform [35]. The penetration of mixing to a certain depth (the mixed layer depth, MLD) is determined by a balance between the stability of the sea water and the incoming energy [36]. Mixed layer is of extreme importance for phytoplankton since if it is much deeper than the euphotic zone, the phytoplankton will have not enough light, while if it is too low, there will be a poor quantity of nutrients in the euphotic zone. Furthermore, MLD has been proven to be involved in the oceanic production of dimethyl sulphide (DMS; [37]). Two plots of the calculated MLD_1 are depicted in figures 3.2 and 3.3, the MLD_2 is higly correlated to MLD_1.

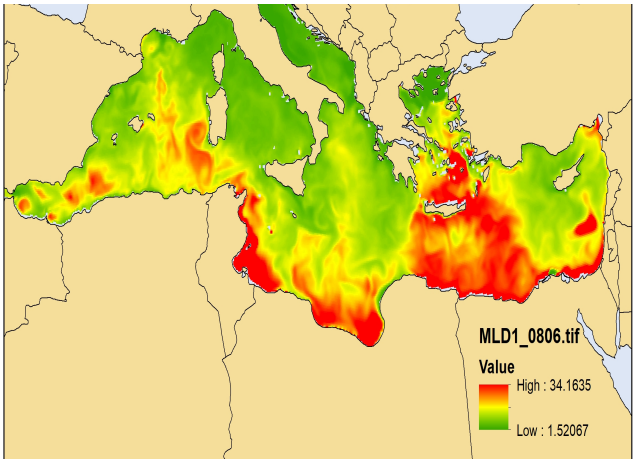

Figure 3.2: An heat map of the calculated MLD_1 for the month of June 2008.

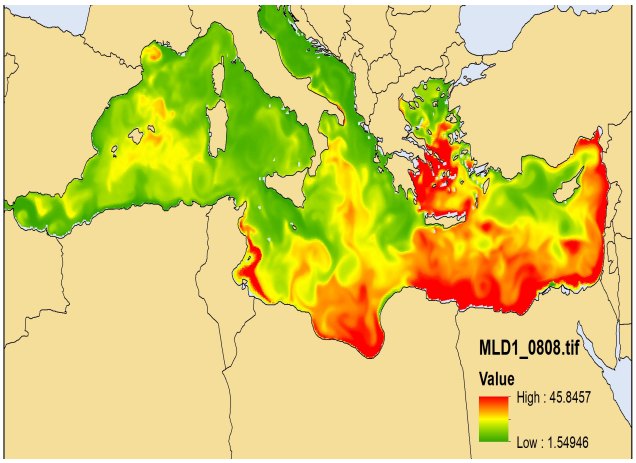

Figure 3.3: An heat map of the calculated MLD_1 for the month of August 2008.

3.2 Shearwaters

Pelagic seabirds, and among them shearwaters, offer a peculiar case for studying behavioural responses to temporal and spatial variation in resource availability. Shearwaters are long-living birds (the oldest known wild bird in the world is a Manx shearwater breeding on Copeland Island, Northern Ireland, with 55 years old) [38] which can use both environmental characteristics and their own experience to target foraging areas [39]. Thanks to their flight strategy, pelagic seabirds are able to range across oceans for hundreds of kilometers apparently without ecological barriers, supporting the idea that they can likely reach any profitable prey field. Shearwaters come to islands and coastal cliffs only to breed. They visit the colonial breeding sites only at night, preferring moonless nights in order to minimize predation. The birds tend to form life lasting couples. Among the shearwaters we will study the behaviour of animals of the genus *Calonectris* and specifically on the species Cory's shearwater, *C. borealis*, Scopoli's shearwater, *C. diomedea*, Cape Verde shearwater, *C. edwardsii*, 3 of the 4 species of Calonectris. The breeding season, during which they grow a single brood, is unusually long: over one full year in Diomedeidae. Both adult and offspring are very resistant to starvation, allowing parents to perform long-lasting foraging trips during which they target known profitable foraging areas which can be located at hundreds of kilometers from the breeding colony. However, at least during the early chick-rearing, offspring needs to be fed regularly, forcing parents to forage closer to the colony. This behaviour results in a so called dual foraging strategy, where the birds can decide between long and short foraging trips and so between different environmental resources. The dual foraging strategy is more evident for colonies of shearwaters in which the surrounding waters are of bad environmental quality. Longer trips are also more frequent for larger colonies, like Linosa, where the surrounding waters are exploited by a large amount of individuals and so rapidly depleted of available food

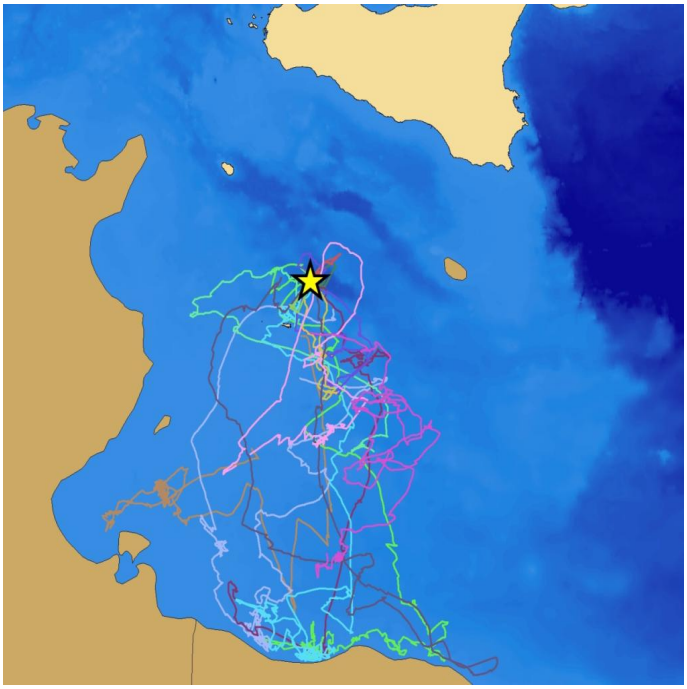

Figure 3.4: Several trajectories of shearwaters from Linosa during self-foraging trips.

resources.

3.3 The relationship between MLD and shearwaters

The study of factors affecting the at-sea distribution of pelagic seabirds has grown during the last ten years mainly thanks to the development of more and more performing tracking technologies, which help scientists to assess ecological aspects that previously could have never been investigated. Despite several studies have assessed the habitat use in procellariiform seabirds (e.g. petrels: [40]; albatrosses: [41]), and a fewer number of studies have focused their attention on at-sea habitat selection or preferences (e.g. petrels: [42]; sherawaters: [39]; albatrosses: [43]), the variation of ecological needs through the long lasting breeding season of these procellariiform seabirds

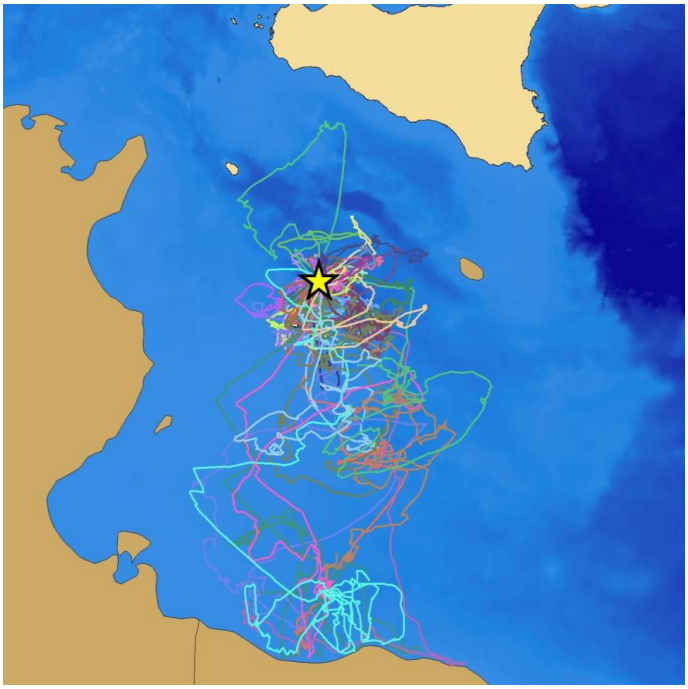

Figure 3.5: Several trajectories of shearwaters from Linosa during chicken-rearing trips.

is a poorly investigated issue of potentially high relevance for conservation purposes. Resource availability is one of the main factors driving the ecology and the biology of animal species. It can have important effects on demography [44], breeding success [45], physiology [46], and of course on distribution [47] and habitat use [48].

One of the main reasons that makes it challenging to carry out studies on habitat preference of seabirds is represented by the difficulty in obtaining a good number of spatially explicit variables which can potentially describe movement patterns of pelagic seabirds across the apparently featureless marine environment. Given the difficulty to have distribution maps of prey abundance covering all the range potentially exploited by pelagic birds, researchers are often forced to use remote sensing information which can play as proxy for prey abundance. Chlorophyll-a concentration, as a proxy of primary production, sea surface temperature, indicating water masses dis-

tribution, baroclinic currents and fronts, and net primary productivity, which might be relevant for determining the availability of small pelagic fishes [49], are the most used variables to model at-sea distribution of pelagic seabirds (for a review see [50]. However, also the mixed layer depth may have a role in determining seabird selection of foraging areas, as it is linked to the distribution of pelagic fishes spawning areas [51, 52] and it is involved in the oceanic production of dimethyl sulphide, which is known to be used by procellariiform seabirds as a cue for both ocean navigation as presented in section 4 and for spotting productive areas [53]. Moreover, the mixed layer depth influences all the ecological food web, starting from roots namely the phytoplankton, as already mentioned. It is quite surprising that to date any studies have used mixed layer depth to model the at-sea distribution of seabirds, and confronted it with other possible predictors like, sea depth, physical oceanographic characteristics (such as shelf edges, frontal zones, and upwellings; [54], concentration of fishing vessels (because of the exploitation of fish discards [55, 39]) or social constraints acting as intra-specific competition [56] and variation in parental care with offspring age [57].

3.4 The MLD extimation

There are numerous methods for estimating the MLD from profile data (see [58] for a review). For the purpose of this study we used two threshold methods, both based on potential density ρ^{θ} (see below) as estimator, which is considered preferable to other parameters because the density structure directly affects the stability and degree of turbulent mixing in the water column [58]. The first method defines the base of the mixed layer as the depth at which ρ^{θ} is 0.01 kg/m3 higher than the surface value (herewith called MLD_1; [59]). This is the standard method for MLD estimation, however this definition is probably too narrow for biological applications, since it often neglects the underlying water of near-identical density encompassing

high chlorophyll, nutrient, and particle concentrations [58]. Therefore we also took into consideration a second threshold difference method (MLD_2; used in the NOAA climatology, [60]) with the potential density threshold set to 0.125 kg/m^3. For MLD estimation, we obtained high resolution maps of 3D monthly mean fields of potential temperature and salinity in the Mediterranean from the Copernicus Marine Environment Monitoring Service website [61]. This product originates from a 60-year reanalysis of the physical state of the Mediterranean Sea that has been produced by combining, every day, the output of an ocean model (Nucleos for European Modelling of the Ocean, NEMO) and quality controlled ocean observations. The model horizontal grid resolution is 0.0625° (ca. 6-7 km), while the vertical grid is composed of 72 unevenly spaced vertical levels (from -5500.0 m to 0 m; as an example, between -100 m and the surface there are 17 levels;). For each pixel we computed the seawater pressure corresponding to the depth value of each vertical level, using the formula described by [62], that takes into account the gravity variation with latitude and the atmospheric pressure, while assuming an ocean water column at 0°C and with a salinity of 35 PSU. Given the values of salinity, temperature and pressure, we then computed for each 3D pixel the potential density ρ^{θ}, defined as the density that a fluid parcel would have if its pressure was changed to a fixed reference pressure p_r in an isentropic and isohaline manner [63], using the *gsw* package (Gibbs Sea Water Functions) in R. Finally, we estimated the MLD_1 and MLD_2 as defined above, interpolating the potential density value between vertical levels when required.

3.5 Identification of behavioural modes

In order to find foraging behaviours in the shearwaters trajectories, we followed a thresholding procedure in velocity and turning behaviour, supposing that movements related to searching and foraging behaviour are the segments

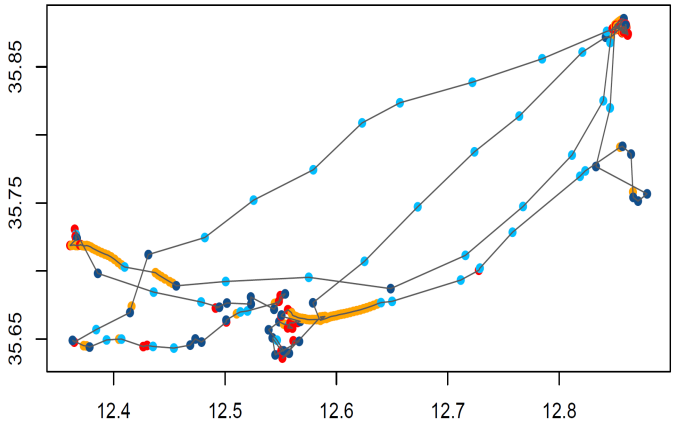

Figure 3.6: One of the birds trajectories labeled.

characterized by low velocities and large turning angles. In order to estimate the proper thresholds, we used as classification algorithm the Expectation-Maximization Binary Clustering (EMbC), an algorithm based on the maximum likelihood estimation of a Gaussian mixture model [64]. This method allows to identify behavioural modes in animal trajectories, minimizing prior assumptions and computational costs, making it particularly suitable to the behavioural annotation of large amounts of movement data [64]. With the EMbC algorithm the whole set of data is partitioned by a set of delimiters that split each movement variable into a binary discretization (either low (L) or high (H) values). In our case, we based our classification on velocity and turning angles. Following [65], we interpreted the labeling as follows: low velocities and low turns (LL) as resting on the water, low velocities and high turns (LH) as intensive search, high velocities and low turns (HL) as relocation, and high velocities and high turns (HH) as extensive search. We then applied a post-processing smoothing implemented in the *EMbC* package and based on the temporal behavioural correlations to minimize the case of incorrect labeling of single localizations. A figure that shows the points of the trajectory labeled is presented in figure 3.6.

3.6 Preparing data for fit

Localizations classified as "intensive search" were used as "use of habitat" points, while the ones labeled as "relocation" were considered as "non-use" points. During relocation, in fact, tracked birds fly over marine areas without slowing down and searching for food, likely for the absence of profitable food sources or other environmental characteristics that favour searching behaviour. Hence, this behavioural mode can be actually considered as non-use of habitat. One advantage of using these localizations as control points is that they have virtually the same distribution of distances from Linosa island as the "use of habitat" points, and therefore it was not necessary to include any kind of constraint, e.g. physical or social, as potential predictor.

3.6.1 Results

Among all the polynomial relationships tested between the searching-nonsearching points and MLD_1 and MLD_2, the best AIC was obtained with a linear relationship: $search = a + bMLD_1$. The best fit results are reported in table 3.1.

	Estimate	P
Intercept	-2.06 ± 0.08	< 0.0001
MLD_1	0.18 ± 0.08	0.0246

Table 3.1: Selected model for chick-provisioning trips

3.7 Including all the environmental predictors

The MLD has correlations with other variables, for example a negative correlation with distance from mainlands and a positive with the sea depth,

meaning that the fit presented in table 3.1 can be just a spurious effect. Therefore, a more comprehensive analysis using other potential candidate variables for the foraging site selection has to be done. In order to perform that, apart from the MLD, we selected 8 other predictors for the analysis of environmental suitability for Scopoli's shearwater in the Sicily channel: (1) sea depth, (2) sea surface temperature, (3) Chlorophyll-a concentration, (4) net primary productivity, (5) distance to the coast (mainland and main islands), (6) an index of distance from fishing harbors as a proxy for availability of fish discards which are exploited by shearwaters, (7) the distance from the breeding colony (herewith called DB), and (8) an index of distance from other Scopoli's Shearwater colonies as a proxy for intra-specific competition. All remote-sensing derived variables were acquired on a monthly scale according to tracking data. Sea depth, SD, was obtained from the General Bathymetric Chart of the Oceans (GEBCO 08) of the British Oceanographic Data Centre [66]as a 30 arc-second grid (approx. 1 km). Monthly data (level 3) of Chlorophyll-a concentration (herewith called CHL) and sea surface temperature (herewith called SST) were downloaded from the NASA's OceanColor website [67]for a spatial resolution of 4 km. Monthly net primary production (herewith called NPP) data (standard Vertically Generalized Production Model based on monthly MODIS-aqua r2009) were downloaded from the Ocean Productivity site [68] for a spatial resolution of 10 minutes (approx. 18 km). For successive analyses, the values of NPP were log-transformed ($log(NPP)$; [39]).

GLMMs [69] were performed in R with the *glmer* function of the "lme4" package. We used a binomial error distribution and a logit model link function. To account for model selection uncertainty, all models with a substantial support ($\Delta AIC_c \leq 4$) were considered, then models performing worse than any of their nested sub-models were discarded as likely containing uninformative variables. The area under the ROC curve (AUC) was calculated

to measure accuracy of the model.

3.7.1 Results

Best-performing model for self-provisioning trips included only the distance to fishing harbors (D_H), with a significant selection of areas closer to harbors. Other models with a substantial support included a significant positive effect of MLD_1 and non-significant effects of distance to the coast D_C and sea depth, see table 3.2. These results confirm the results of section 3.6.1. It is interesting that the next values selected are D_C and SD, both correlated with MLD_1. On the other hand, the model selected for chick-provisioning trips included only sea depth in the quadratic form, with a significant selection of both shallower and deeper waters 3.3. This is not surprising since, as already mentioned, chick-provisioning trips are usually shorter, and shearwaters cannot reach high quality foraging grounds. Also the disappearance of the harbor distance is not surprising since boat-fish discharges[1] are bad quality food not suitable for breeding.

	Estimate	P
Intercept	-1.98 ± 0.08	< 0.0001
D_H	-0.41 ± 0.15	0.006
MLD_1	0.18 ± 0.08	0.02
D_C	-0.15 ± 0.09	0.09
SD	0.12 ± 0.08	0.13

Table 3.2: Model-averaged coefficients for self-provisioning trips.

[1] except for anchovies, where entire fishes are discharged just for law or market reason

	Estimate	P
Intercept	-2.21 ± 0.17	< 0.0001
SD	0.50 ± 0.21	0.018
SD^2	0.36 ± 0.11	< 0.001

Table 3.3: Selected model for chick-provisioning trips.

3.8 Conclusions

In the present study, we show that foraging habitat preferences of Scopoli's shearwaters changed during the breeding period according to foraging trip types. Habitat selection models showed that the probability of intensive search behaviour during self-provisioning trips was higher in areas closer to harbours and with a deeper mixed layer, while it mainly depended on sea depth during offspring-provisioning. These results suggest that the species is able to vary the prey item target in accordance with the environmental characteristics of the exploited habitats. The preference for areas in the proximity to a high number of fishing harbours or to harbours with large fishing fleets during self-provisioning trips may be explained by the higher probability to find, in such areas, fishing vessels throwing discards due to the fish processing during the returning trip. Vessels and discarding location behave indeed as central-place foragers, where the harbour represents the "central place". This result is in accordance with [39] which showed that long-distance trips performed during incubation are undertaken by Scopoli's shearwaters to forage close to fishing harbours, suggesting that these areas represent profitable locations which may compensate for the greater travelling costs. The consumption of fish discards by Scopoli's Shearwaters has been also described by [70], as well as for another shearwater species breeding in the Mediterranean, the Balearic Shearwaters foraging off the Ebro Delta [71]. While the relation with fishing harbours was expected, the preference

for deeper mixed layer represents a novelty in the knowledge of pelagic birds ecology. Despite shallower mixed layer in the ocean is associated to a higher density of phytoplankton [72], in the Mediterranean deeper mixed layer are areas of plankton retention and are associated to the presence of anchovy and sardine in the central Mediterranean (see [73] for a study in the Aegean Sea). These small pelagic fish species are indeed key prey items for Scopoli's shearwater [74]. Overall, the analysis of habitat preference during long-distance trips suggested that the Scopoli's shearwater targets two different resources during self-provisioning, i.e. fish discards and small pelagic fishes. It has been shown that, for another pelagic bird species, the Cape Gannets *Morus capensis*, non-breeding individuals can complement their diet with fishery discards but that nestlings fed with fishery wastes have a lower probability of survival [75]. During long-lasting foraging trips (corresponding to long-distance trips, [76]), shearwaters exploit profitable areas so as to both restore their own physical condition and obtain larger meals for their offspring [77, 78]. Thus, we can conjecture that areas close to fishing harbours are mainly used by breeders to forage on discards and restore themselves after long trips, while deeper mixed layer areas are used to feed on natural preys, which might also be used to feed nestlings after hatching.

During offspring-provisioning trips, in fact, areas closer to fishing harbours are no longer preferred, likely because they are not easy to reach in such a short time ($<$4 days) or because fishery discards do not represent a resource of sufficient quality for their nestlings. The selection of foraging areas during these trips only depended on sea depth, but with a not linear relationship. Shearwaters are in fact more likely to search for food in both deeper and shallower water, possibly suggesting the exploitation of two different resources. Close association to shallow waters has been reported for different species of sardines [73, 79], in particular for young (of the year) fishes which dominate the sardine population during early summer in the Mediterranean.

On the other hand, the selection of deeper waters finds no easy explanation. Despite shearwater diet is mainly based on pelagic fishes [74], recent studies suggest that Scopoli's shearwater breeding in the Mediterranean coasts may also feed on planktonic crustaceans (krill) or fish larvae [80, 75]. Thus, the exploitation of deeper waters by shearwaters might be due to the markedly increasing species-richness gradient of krill from coastal to offshore areas [81].

Overall, these results support the foraging plasticity of Calonectris shearwaters [82, 74] and the importance to consider all to plan management and conservation actions targeting the species.

The MLD has been shown to be an important factor in determining the habitat selection of shearwaters and should be included in all successive studies of the habitat of pelagic animals and in particular of pelagic birds. It is worth noting that the MLD is a quantity that varies in space and time and with our reanalysis we couldn't capture fully its dynamics. Among the predictors used is the one affected by the greatest error: it relies on empirical formulas, applied on monthly averaged data that are results of a reconstruction. Therefore, on small temporal trips and shorter scales, the MLD is the predictor more difficult to estimate. We expect that a finer resolution in this quantity will be extremely helpful in determining the effect of MLD on habitat selection, possibly enhancing the prediction power of this quantity on habitat selection of shearwaters. Overall this work is another example of how physical processes and reanalysis based on physical modelling are becoming key elements in biological science.

Chapter 4

Macro scales

After foraging in the open ocean pelagic birds can pinpoint their breeding colonies, located on remote islands in visually featureless seascapes. This remarkable ability to navigate over vast distances has been attributed to the birds being able to learn an olfactory map on the basis of wind-borne odors. Odor-cued navigation has been linked mechanistically to displacements with exponentially-truncated power-law distributions that are expected to be wind dependent. In this chapter, we will show that the pdf of unidirectional flights in shearwaters is compatible with the expected one. Later we will show that the distributions are wind-speed dependent, in accordance with theoretical expectations, providing strong evidence of odour-cued navigation in shearwaters. Our novel analysis is consistent with the results of more traditional, non-mathematical, invasive methods and thereby provides independent evidence for olfactory-cued navigation in wild birds.

4.1 Introduction to animals movement patterns

In all fields of science, several phenomena can be described, at a macroscopic level, by a Gaussian distribution. This ubiquity is due to the central limit theorem, which states that when independent identical random vari-

ables with finite variance are added, the distribution of their sum converges to a Gaussian. Brownian motion (BM) itself is a result of the central limit theorem: in a viscous fluid, a large number N of iid impulses to a particle bring to a particle displacement Gaussianly distributed. BM was the starting point for the study of Random walks, namely a path that consists of a succession of random steps where every step i is characterized by a $\boldsymbol{r}_i$ taken from a probability function $\phi(\boldsymbol{r}_i)$. The most simple case is a Markovian process, with $\phi(\boldsymbol{r})$ being isotropic and with a unique step length, namely $|\boldsymbol{r}| = l$. The Donsker's theorem states that in the limit of $l \to 0$ the random walk, defined before, is indistinguishable from a Wiener process, and therefore to a BM in the over-damped regime. Although at large scales many animal trajectory data resemble Brownian motion, at low scales is evident that uncorrelated random walks cannot describe animal motion, since a degree of directional persistence should be present. In order to include directional persistence on short scales, Correlated Random Walks (CRW) are usually used to describe the movement pattern of many animals [83, 84]. Restricting our analysis to two-dimensional random walk, a CRW can be defined choosing a non-uniform distribution of the angles θ_i between two displacements $\boldsymbol{r}_i, \boldsymbol{r}_{i+1}$. Maintaining Markovianity, we can just specify a pdf for the angles θ. If the angle pdf is symmetric, we can define the mean angle $\rho =< \cos(\theta) >$ and it is possible to find that the correlation time is proportional to $-1/\ln\rho$ and that the autocorrelation function decays exponentially. Therefore, CRW is characterized by a spatial (or temporal) scale, namely the scale after which the walk becomes uncorrelated. Therefore, at large scale, there is no difference between CRW and BM, a result due to the exponential decay presents in the correlation function of CRW. A simpler model that mimics the CRW in achieving temporal persistence in movement pattern, is obtained specifying a pdf in step length exponentially distributed. This model is more suitable to be generalized to multi-scale movement patterns, namely movement patterns

with more than a scale. This can be easily obtained by specifying a multimodal pdf of step lengths or summing more exponentials with different scale lengths. Bi-scale (or even 3 scales) movement patterns are common in nature and particularly important for animal performing searches. Mono-scale movement patterns are indeed characterized by a great degree of redundancy in visited places, a characteristic that in case of not renewable targets is time consuming and so biologically not advantageous. Multi-scale movement patterns instead can alternate short scale compact search and long distance relocation, greatly reducing redundancy in visited places.

4.2 Lévy walks

Distributions with not finite variance have been reported, for example in the field of physics in turbulence, as we already saw, and more notoriously in phase transitions, while in geology it is very well known for the pdf of earthquakes. Despite these famous examples, in fields like biology or economics, distributions with not finite variance were relegated for decades as pure mathematical models and only recently had become notorious with many fertile applications. Lévy walks, that are also known as Lévy flights in the biological literature (a fact that confuses the communications between biologists and mathematicians/physicists), named after the French mathematician Paul Lévy, are defined as random walks in which the step-lengths have a probability distribution that is heavy-tailed[1]. Among the distributions with infinite variance, power laws, namely distributions that up to a certain minimum x can be expressed as x^{μ} are the most studied and applied due to their simplicity and some interesting properties, like scale invariance. In order to be a power law, the power-law exponent μ has to satisfy $1 < \mu \leq 3$, ensuring

[1] An heavy-tailed distribution is a distribution in which one side of the probability distribution is not exponentially bounded. In particular, we will be interested only in the right side of the distribution.

that the distribution is normalizable and has a divergent variance. The first finding of a Lévy walk in movement ecology was the famous article by [85] on wandering albatross. The author explains this result stressing that Lévy walks are characterized by super-diffusivity, fractality, and scale invariance and therefore compared to CRW, Lévy walks reduce the possibility of visiting multiple time the same location, a property surely advantageous in a search. Later demonstrated this result [86] showing that Lévy walks with exponent $\mu = 2$ are optimal for searching random diluted sources compared to CRW. A new paradigm, the so-called Lévy Flight Optimal Foraging Hypothesis (LFOFH), stating that "Since Lévy flights and walks can optimize search efficiencies, therefore natural selection should have led to adaptations for Lévy flight foraging", was forged. These findings brought a lot of attention on Lévy walks and many reports of Lévy Walks appear.

Unfortunately, the concept of Lévy walks is prone to be misunderstood by researchers not familiar with pure mathematics, and special care has to be used in analysing the data. As a result, many reports of Lévy walks resulted flawed, including the seminal study of Viswanathan [85], leaving the doubt of the validity at all of this model in movement ecology. However, a complete re-analysis confirmed compelling evidence that movement patterns of many organisms can be described as Lévy walks, although with a cut off at some higher scale, as cells, mollusc, microorganisms, insects, fishes, and birds.

4.3 How to determine if a movement pattern is a Lévy walk

Given an animal trajectory, firstly we have to identify the turning points, namely the points where the animals change their direction of motion. This procedure, that naively can be thought to be very easy, hides several difficulties. Animal trajectory data are usual GPS-track data that suffer from

a trade-off between battery charge duration and period of fixes, meaning that the accuracy of the recorded data can be not enough to reconstruct exactly the original pdf. Moreover, if the researcher is interested in large-scale movement, the small-scale pattern of animals, like bypass an obstacle, can deeply influence the results if not properly filtered away. The procedure on how identifying turning points is therefore still an active field of research [83] and several methods are reported in the literature, and general objective methods have still to be found. Once the turning points are obtained, if the speed of the animal is constant (we have to note that this is a prerequisite for a Lévy walk), we can analyze the pdf of the lengths of the unidirectional steps.

If high noise at small scales is present, the distributions can be cut at low scales, but extra care should be taken in order to not eliminate significative signal as in [87]. Afterward, the distribution is compared to other model distributions reported in the literature, like exponential or bi-exponential. The parameters of every proposed model are fitted via Maximum likelihood methods and then the models are compared via AIC. If the difference in AIC is significative in favor of the Lévy walk, then evidence of Lévy walk are present and reported. Moreover, other parameters like mean square displacement can be fitted in order to confirm the model. It is important to mention that pure Lévy walks are very improbable in a living system. Physical constraints are usually present, like diurnal cycles or land-sea distributions that can cut the distribution. This cut off is usually visible present in all the before mentioned findings and therefore the model fitted is not a pure power-law but instead a power-law with some sort of cut-off like for example an exponential cut off.

4.4 Shearwaters, beyond Lévy walks and the LFOFH

Shearwaters are pelagic birds as the albatross, the exemplary animal of Lévy walks. Shearwaters during the breeding season are forced to go to the foraging points and return back to their colony often localized in a small remote island. For humans, the open ocean is mostly featureless, meaning that we cannot pinpoint ourselves in a map just looking at the sea. It is important to stress that being able to orientate, for example using the sun, is different to pinpoint on a map and hence shearwaters need to have some navigation mechanism. Homing experiments [88] conducted on shearwaters evidence an important role of olfaction. In these experiments, shearwaters were brought far away from their breeding colony and then released. Apart from the control group, some birds were manipulated to be made anosmic, while others have magnets attached. Anosmic birds take more time to reach home and their trajectories are visibly and statistically different [88]. In the article [89] the authors analysed the GPS tracks data of shearwaters. The Shearwaters were of different species and come from different colonies in different environments. Analyzing the step lengths distribution of unidirectional flights of shearwaters, they brought evidence of a power law with an exponential cut off and power-law exponent μ around -3/2. The explanation of the authors is that shearwaters have a map of odours and rely on that for navigation, although the map can be dynamical in time. In open sea various odours are produced, among them the already cited DMS, depending on the marine populations in the waters. Then, odours are transported over long distances by the mean wind and heavily distorted by the associated turbulence. Therefore, the birds can get information on their position, both when they are over the odour source or when they are downwind to it. Obviously, shearwaters cannot perceive odour under a certain threshold and therefore, in some moments, they lose contact with their odour map. This is due to turbulence; several experiments measured the time statistic

of scalar concentration released from a source and advected by a turbulent flow with a mean direction. This statistic, downwind and far enough from the scalar source, becomes highly irregular. Of particular importance for us is the statistic of periods over and under a defined threshold. In the article [89], the authors calculated analytically this statistic by means of some assumptions for the case of a small source, where small is related to the flow scales, and verified their prediction by means of numerical simulations. One of the main prediction of the models presented in the article is that periods over the threshold are characterized by a power law with exponent -3/2, an exponential cut-off at high scale and a cut off of non-specified form at low scales. In order to elucidate the findings of [89], we will try to explain their results with a simple stochastic model for time-series of odour concentrations. Let suppose that incremental changes in concentration are of the form $dc = a(c,t)dt + b(c,t)dW$ where $a(c,t)$ is a relaxation term and $b(c,t)$ is the magnitude of the driving stochastic noise, dW is the driving stochastic noise (let suppose an incremental white noise process). Therefore it follows the associated Fokker-Planck Equation:

$$\frac{\partial p(c)}{\partial t} = a(c,t)\frac{\partial p(c)}{\partial c} + \frac{b^2(c,t)}{2}\frac{\partial^2 p(c)}{\partial c^2} \tag{4.1}$$

If $a(c,t) = -c/T$ and $b(c,t)$ is constant, then we have the standard Langevin equation and it can be shown that the distribution of odour concentrations, $p(c)$ is Gaussian. Generally, the Fokker-Planck Equation (FPE) determines the relationship between $a(c,t)$, $b(c,t)$ and $p(c)$. Specifying $a(c,t)$ and $b(c,t)$, the FPE gives us $p(c)$, while specifying $p(c)$, the FPE gives us $a(c,t)$ and $b(c,t)$. Experimental observations report that odour concentrations in turbulent flows follow a clipped-Gaussian distribution [90]; however let us suppose for the moment an exponential distribution for $p(c)$. The associated FPE is then given by

$$\frac{\partial p(c)}{\partial t} = \frac{C}{T}\frac{\partial p(c)}{\partial c} + \frac{C^2}{T}\frac{\partial^2 p(c)}{\partial c^2} \tag{4.2}$$

where T is the autocorrelation timescale, i.e. the typical durations over which concentrations remain significantly correlated, and C is the mean odour concentration over time. From this equation can be demonstrated that the time τ over threshold c_{th} starting from an initial point c_0 is distributed as:

$$p(\tau) = N\tau^{-3/2}e^{-\lambda_1\tau}e^{-\lambda_2/\tau} \tag{4.3}$$

where N is a normalization constant,

$$\lambda_1 \propto 1/T \tag{4.4}$$

and

$$\lambda_2 \propto T\frac{(c_0 - c_{th})^2}{C^2}. \tag{4.5}$$

An analogous result can be found for the distribution of durations during which concentrations remain continually above some threshold concentration. A doubly exponentially truncated power law can be obtained also assuming a Gaussian distribution of odours (see subsection B.2.1 in Appendix). The power law behaviour, $\tau^{-3/2}$ is a manifestation of the Sparre Andersen Theorem [91] and so generic rather than model specific. We have seen so far that an exponential cut off at large scale and a power law behaviour with exponent $-3/2$ is expected in all the models considered. A cut-off is expected also at short scales, but its exact form is model dependent. In [92] the cut off scales are related to the mean wind, the distance from the source, its dimension, and even the lateral displacement. In the simple example mentioned before, we expect both T and C to be dependent on atmospheric conditions, and especially on the mean wind speed. The existence of such dependence can be seen with the aid of a simple heuristic argument. Imagine, for example, a patch of ocean with area L^2 releasing odor into the atmosphere at a rate F which subsequently becomes dispersed by turbulence up to a height H in the atmospheric boundary-layer. The total quantity of odor released from the patch during a time interval of duration t is $Q = FL^2t$ and this

will become distributed throughout a volume of air $V = LHUt$, where U is the wind speed. The mean odor concentration is then $C = Q/V \propto F/U$. According to [93], empirical observations suggest that the flux of DMS and so presumably other volatiles is itself dependent upon the mean wind speed, such that $F \propto U^{\gamma}$ where estimates for the characteristic exponent, γ, range between about 2 and 3. The autocorrelation timescale will also depend on the mean wind speed U. Hence λ_1 and λ_2 must also depend on the mean wind speed because they depend on the autocorrelation time scale and the mean odour concentration.

Going back to the shearwaters, we can suppose that they will follow unidirectional flights when they are in a puff of odour over threshold while they will try to re-establish contact with the odour map when they are experiencing a period under threshold. We can then suppose that their unidirectional flight length distribution to be distributed as

$$p(l) = Nl^{-3/2}e^{-\lambda_1 l}e^{-\lambda_2/l} \tag{4.6}$$

with λ_1 inversely related to the time scale T and λ_2 depending on the atmospheric conditions. We have to stress that odour navigation is not an accepted paradigm in the scientific community. Many researchers favour the magnetic navigation hypothesis. The different behaviours found in experiments conducted on anosmic birds might be explained by reasoning that in the manipulating the birds in order to make them anosmic, the birds lose both smell and magnetic senses. Therefore, a mechanistic demonstration of olfactory-cued navigation in shearwaters is necessary. In order to verify our model, we perform an MLE estimation of the parameter mu,λ_1 and λ_2 of the function

$$p(l) = Nl^{-\mu}e^{-\lambda_1 l}e^{-\lambda_2/l} \tag{4.7}$$

on step length distribution of unidirectional flight lengths of each individual bird trajectory. Successively we verified that:

- BETPL are better fits of the step length distributions than the other distributions proposed in the literature to model movement patterns of birds.
- $\mu = -3/2$
- λ_1 is negatively related to the wind, namely we expect $\lambda_1 \propto U^{\beta_1}$ with $\beta_1 \sim -1$
- λ_2 depends on the wind, where heuristic arguments suggest a negative dependence[2], namely $\lambda_2 \propto U^{\beta_2}$ with $0 < \beta_2 < -2$.

4.5 Hypotheses testing

We collect GPS track data of birds from different colonies: three Mediterranean colonies: Linosa island (35° 52′ N; 12° 52′ E), the Tremiti Archipelago (42° 08′ N; 15° 31′ E), and La Maddalena Archipelago (41° 13′ N; 9° 24′E) and three north Atlantic islands: Corvo (39° 40′ N; 31° 06′ W), Berlenga (39° 24′N; 9° 30′W) and Selvagem Grande (30° 08′N; 15° 51′W) and Raso islet (16° 36′N; 24° 35′W). We downloaded wind data from the NOAA [94] web site from the rerdapp [95] package for R [96]. The data comes from satellite measurements, have a spatial resolution of 0.5 degrees and time resolution of 6 hours and are indicative of the wind speed at 10 meters above the sea level. We perform for each wind direction a simple linear interpolation in space and time in order to estimate the wind speed at the spatiotemporal coordinates of the birds (other methods like inverse distance weighted or spline were tested on a subset and lead to not relevant differences). We compare our model with competing models such a bi-exponential, simple power

[2]The dependence of λ_2 on the mean wind is more difficult to estimate because it depends on the details on the source like how the flux is increased by the wind, a complicated mechanism that has to include the presence of waves, water bubbles in air, air bubbles in water, the MLD etc...

laws, a power law with only high scale truncation, simple exponential and another distribution obtained by the sum of a BETPL and an exponential. These alternative models have been clearly observed across taxa and are biological meaningful: a good fit to a bi-exponential would indicate a bimodal search; a good fit to a power law would indicate a Lévy search pattern; an exponential would be indicative of a single-scale search. BETPL are better supported than all other models (more), while the second best model is the bi-exponential, in particular, the BETPL for trips longer than 3 days outperforms the bi-exponential in the 89% of cases.

The first prediction of our model is that μ, the exponent of the power law in BETPL, is $3/2$ and is independent of the wind. In Figure 4.1, we plot the fitted μ of every trip against the maximum displacement from the colony. The estimated μ value converges to the predicted value $3/2$ as the displacement increases.

A similar result can be obtained using the duration of the trip as independent variable, as we known that trip duration is correlated with the maximum distance from the colony [76]. These convergences are due to the increase of statistical power. As predicted, correlation between the mean wind and the fitted μ are very low ($r = 0.12$, $P = 0.23$, df=108) and no pattern is evident by visual inspection.

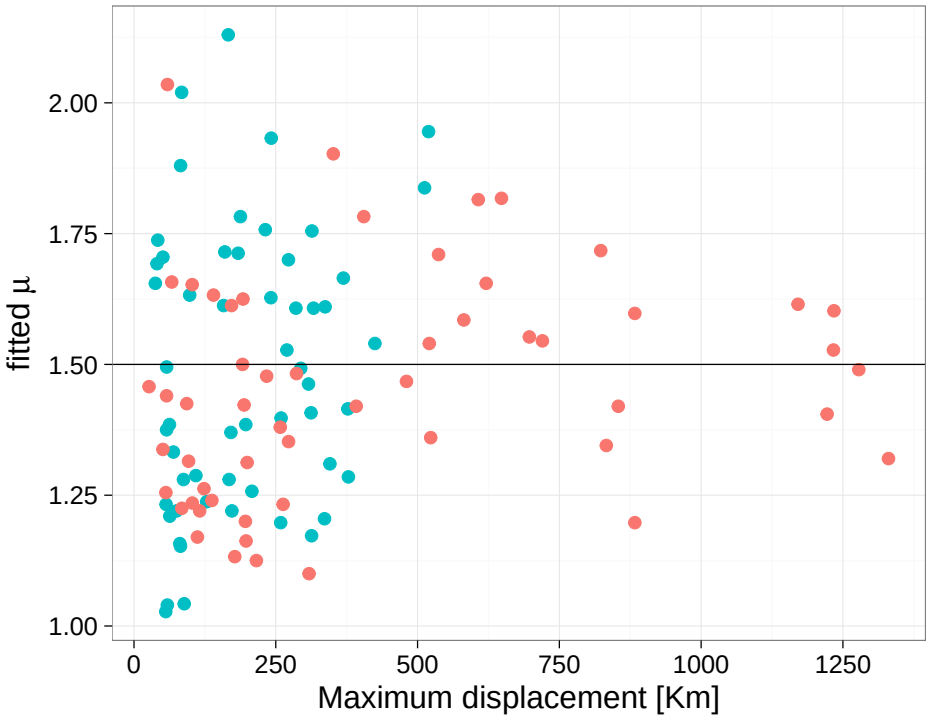

Figure 4.1: Fitted value of μ plotted against the maximum displacement reached from the colony. The horizontal line is the predicted value for μ. Data relative to seven colonies in the Atlantic ocean (Red dots) and in the Mediterranean sea (Blue dots).

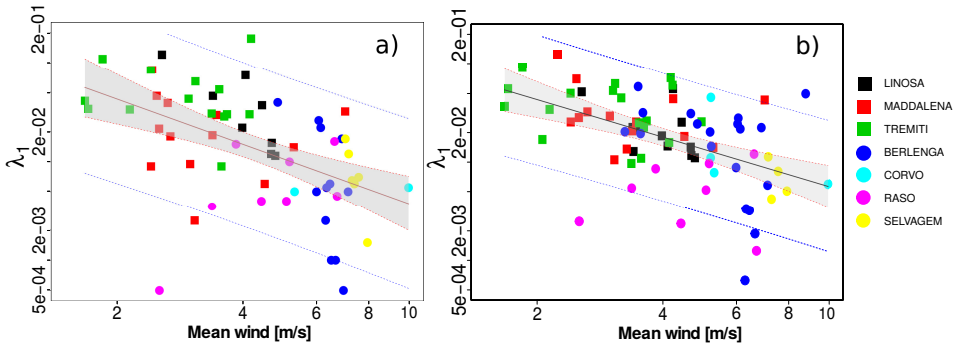

Figure 4.2: Data relative to seven colonies in the Atlantic ocean (dots) and in the Mediterranean sea (squares). (a) Log-log plot of the mean wind against λ_1 for trajectories that last more than 4 days. (b) Log-log plot of the mean wind speed against λ_1 fitted with $\mu = 3/2$ for trajectories that last more than 2 days. The blue line is the 95% confidence limits for the mean predicted values and the red line is the 95% confidence limits of the individual predicted values.

Since the prediction of the relationship of λ_1 with the wind is expected to be of inverse proportionality, we perform the fit $\lambda_1 \sim U^{\beta_1}$. Figure 4.2a shows a log-log plot of the fitted λ_1 over the mean wind speed for trips that last more than 4 days. The fitted regression coefficient is negative and highly significant ($\beta_1 = -1.5 \pm 0.3$, $P < 0.0001$). As it can be seen, the fit is clear although some outliers are clearly present. These outliers are perfectly explained since the MLE estimation of λ_1, λ_2 and μ is highly noisy, as demonstrated in a previous analysis performed on synthetic data. In order to reduce the noise on λ_1 and λ_2, we, therefore, perform a second MLE estimation of the parameter of the BETPL on the step length distributions blocking $\mu = -3/2$, the expected value. The fit of these new values of λ_1 on the mean wind is depicted in figure 4.2b and the resulting fitted β_1 is -1.26 ± 0.26 ($P < 0.0001$). From the analysis of synthetic data, we found that the noise is particularly high in the estimation of λ_2. On the MLE

estimations of λ_2 obtained blocking $\mu = -3/2$, we perform a fit $\lambda_2 \sim U^{\beta_2}$. Although very noisy, the fit indicates a clear negative β_2 ($-0.7 \pm 0.3, P = 0.012$, df=43). Therefore, we brought new strong evidence for odour cued navigation in shearwaters.

4.5.1 Possible mechanistic wind effect

We have tested the eventual presence of a direct effect of wind speed on truncation parameters independently of odour cued navigation in appendix B.2.2. We found a scarce, albeit significant, effect of wind speed of both head- and tail- winds on the value of λ_1 while λ_2 appears unaffected by head- and tail- winds.

4.6 Model validation using data from independent data

Since the article of Edwards [97] a shadow has been cast on the Lévy flight community and many scientists are very skeptical on the subject. In order to provide another independent proof that our methods are useful and correct, they should be able to correctly identify if a bird is or not doing olfactory cued navigation. To challenge our method of data analysis we decided to use the data provided by [88] available from Movebank. These authors investigated the homing performance of Scopoli's shearwaters (*Calonectris diomedea*) breeding at Pianosa island (Italy). The following data were available: 11 anosmic, 8 control and 9 magnetically-disrupted birds (the experimental methods used are fully reported in the original paper). After treatment, birds were released in the Lion Gulf, 400 km west of the colony. The dataset was reduced to meet the statistical exigencies of our analysis because several trajectories were not complete and so were discarded. Thus our sample is constituted by 6 anosmic bird trajectories, 8 control bird trajectories

and 7 magnetically-disrupted bird trajectories. Since in many cases the available statistic was not enough to perform our analysis on an individual basis (the trajectory are quite short in time compared to ours), we decided to pool the trajectories with identical treatment. The pooling produced a statistic of around 1500 step lengths for the anosmic birds, 750 step lengths for the control group birds, and 770 step lengths for the magnetically disrupted birds. We fit the data with the double exponentially truncated Lévy model and the goodness-of-fit was tested using the Kolmogorov-Smirnov test weighted for tails, KS_{tail}. Results are displayed in Figure 4.3.

The KS_{tail} gof values get stable for $lim_a > 0.25$ km. It is clear that control birds outperform the test with respect to anosmic birds and at some extent with respect to magnetically disrupted birds. We wish to stress that such results are derived using exactly the same software which was employed for the analyses in our paper. Using an independent dataset, this result confirms that our modelling approach is able to identify the presence of olfactory navigation under natural conditions discriminating trajectories of birds using olfactory navigation from birds using different navigation mechanisms. Both our analysis and the one by [88] concur to the same conclusion that anosmic birds present an impaired navigational mechanism. However, in our analysis magnetic-deprived birds appear closer to anosmic birds while [88] stressed that even magnetic-deprived birds navigate better than anosmic ones. However, we draw attention to the plots relative to the initial orientation of birds (Fig. 3 in [88]) showing the initial homeward orientation. Control birds were well orientated towards the home direction, while anosmic were significantly oriented elsewhere and magnetic-deprived birds were only marginally oriented towards home. The bivariate distribution of magnetic-deprived birds appeared to be more scattered than the one of control birds. This pattern fits very well with what we observed. We conclude that both our modelling approach and the experimental approach of [88] get to identical conclusion.

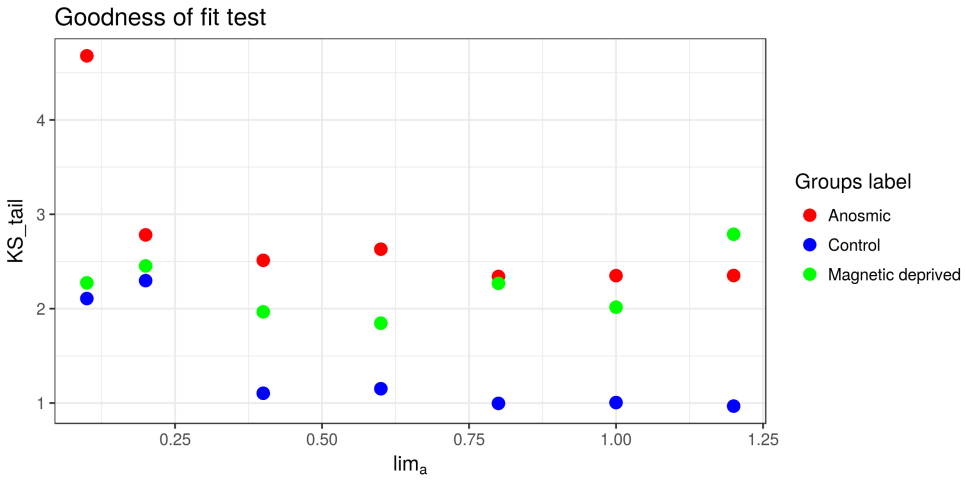

Figure 4.3: We display the Kolmogorov-Smirnoff statistics corrected for tails, KS_{tail}, (smaller is better) (ordinates) as a function of lim_a. The value of lim_a (km) is the value under which we cut the distribution, since there is an intrinsic noise at small scales in GPS tracks and in the identification of step lengths.

4.7 Conclusions

We have therefore shown that at-sea distribution patterns of foraging shearwaters are clearly wind-dependent as suggested by the proposed olfactory navigation mechanism. Our methods of analysis are novel and inspired by a mathematical theory for how odours disperse within the atmospheric boundary-layer and account for the complex ways in which turbulence distorts and disperses packets of odour. The hypothesis that shearwaters rely on odour-cues for navigation then becomes a sharply defined, falsifiable statement about the distribution of flight-segments. Our model distribution contains three parameters. One is uniquely determined by the theory and is a pure number, $3/2$, the other two, λ_1 and λ_2 are predicted to depend on the mean wind speed. It is thus unlikely that good fits to our model predictions can be attributed to other processes. We find that the characteristic power-law exponent μ is clearly distributed around the expected value of

3/2 and is independent of the mean wind speed, as expected, while the other two parameters λ_1 and λ_2 depends on the wind. It is worth noting that these dependencies are not generic ones but are specific to our theory in sign and size. Therefore this results provide clear and compelling evidence of olfactory-cued navigation in shearwaters and bolster significantly the previous findings[89] who did not test for wind-speed dependences and complements the evidence, obtained using more traditional methods [98, 88, 99]. We thereby linked flight patterns to underlying navigation mechanism for the first time. According to the mechanism initially proposed by Kramer and Gustav[100] the navigation should be a very precise and predictable tool: once the animal is able to get its coordinates, can use a compass to attain its target; on the contrary the mechanism we proposed is strongly stochastic since it is influenced by the often unpredictable turbulence of the atmosphere. On one hand, turbulence is indispensable for odour navigation because it carries information to the birds. On the other hand, too much turbulence might reduce the navigation ability due to the high variability of the odour signal. This stochasticity might explain, at least in part, the variability which has been observed in experiments with homing pigeons. Indeed Walraff *et al*[101, Chapter 3.4] concluded that "The angular dispersion of bearings appeared to reflect stochastic noise and is most reasonably compatible with the hypothesis that no one pigeon was able to gain clear-cut information on the direction of home because noise was inherent already in the environmental signals providing positional information". The observed dependencies of λ_1 and λ_2 are crucial for detecting olfactory cued navigation because a μ value of 3/2 can be also determined by other mechanisms. Further evidence that our interpretation is correct is the exclusion from most of the studied trajectories of alternative movement patterns such as simple exponential, bi-exponential, power-law and single truncated power law. To our knowledge, there is no other mechanism which could explain the observed

relationship of λ_1 and λ_2 with wind speed, if olfactory navigation it is not involved. The estimation of λ_2 differently to the estimation of λ_1 suffers from a lack of resolution in our trajectories. Indeed a sampling of 10 minutes is a compromise between resolution and battery duration. Only newest GPS-logger generation may allow for a denser sampling of trajectories which may improve the estimation of λ_2. Small-scale behaviour unrelated to navigation [102] is one such source of noise in the estimated λ_2. Furthermore, our simulations have shown that λ_2 is the most difficult parameter to be estimated. Comparable results were obtained for both λ_1 and λ_2 where tested with different sub-settings, bootstrap and different methods of estimation (data not presented), all leading to comparable results. The mechanistic effect of wind on the flight pattern of shearwaters is not at all unexpected [103] but its effect is much less relevant than the one determined by olfactory-cue navigation.

According to Komolkin *et al.* [104] a bird could use a hierarchy of orientation systems such as geomagnetic navigation at very long distances, olfactory at intermediate scales and piloting for short-range movements. Surprising both Pollonara *et al.* [88] and our study found olfactory navigation in birds from small Tyrrhenian islands, where we could have assumed that piloting can be quite effective. In our study, we confirmed that shearwaters can rely on olfactory maps over distances of several hundreds of kilometres. It would be interesting to analyze the flight patterns of albatrosses that are wandering for thousands of kilometres in the southern oceans and determine whether olfactory navigation is the dominating mechanism also at such scales. Besides the importance of olfactory cued navigation for homing, demonstrated in *Procellariformies* and homing pigeons, recent researches have suggested that lesser black-capped gulls may use olfactory cued navigation during migration [105]. Our model may represent an appropriate tool to investigate this hypothesis on a large number of wild birds, especially when conserva-

tion concerns do not allow for experimental manipulation of a large number of birds. More generally our model may be applied to other taxa such as ants [106], seals and marine turtles where there is evidence for olfactory cued navigation at different spatial scales [107].

Chapter 5

Conclusion and further perspective

In this work we investigated how turbulence affects the nutrient uptake of small organisms, the foraging grounds and the navigation mechanism of shearwaters. We found that the time dynamic present in turbulence flows can enhance the growth rate of small organisms beyond the values predicted using the average values. This result is especially important because it contradicts theoretical arguments that instead predict the opposite. Finally, we provided stronger evidences that the growth rates depicted in the experiments [11] and [12] can not be explained with the turbulence levels reported in the latter. We also found for the first time that sea turbulence, depicted using the MLD, is correlated with foraging spots of shearwaters and therefore with the distribution of their preys. These results are very important for ecological and conservation porpouse and the mixed layer depth should be incorporated in every future analysis in pelagic birds habitat use. Finally, we provided strong evidence for olfactory-cued navigation in shearwaters, relating their pdf of unidirectional flight segments to the air-turbulence depicted by the mean wind. All of the three mentioned topics are extremely valuable of further investigations: a complete investigation of the nutrient

uptake of an elongated motile organism in realistic turbulence is lacking, and altough its numerical complexity, its value for micro-organism marine ecology (and therefore the climate) is crucial. In open ocean the MLD is even more important for the marine ecology and a study of the relationship between the foraging spots of pelagic birds and the MLD for oceanic birds can be very productive. More in general an extension of our study using data from shearwaters from different habitat would show if variables that affects habitat selection in shearwaters are general or geographically dependent and will have the advantage of decrease the overall correlations among the proposed predictors. Our results suffered from a lack of precision in the MLD estimation and therefore repeating the analysis with more refined data would possibly increase the prediction power of the MLD in habitat selection. Finally the odour-cued navigation mechanism that we presented has to be investigated more in depth. Evidences of odour-cued navigation were reported for several other animals beyond shearwaters like ants, seals and marine turtles. Applying the same statistical methods to these animals in a general multi-species analysis can be very interesting. Among the animals performing odour-cued navigation, desert ants can be also suitable for an experimental investigation with the highest degree of experimental control on the odour concentration field, although their navigation mechanism could be very different from the one of shearwaters.

Appendices

Appendix A

The role of time dynamics in fluid flows for nutrients uptake

In this section we will study the role of temporal dynamics in fluid flows in the uptake of a spherical small organism by virtue of some simple illustrative examples. In particular, in order to reduce the numerical complexity while capturing the key temporal ingredients, we shall consider only axi-symmetric linear fluid flows, already defined in eq. 2.10. The Stationary solutions for a stationary general linear flow near to a sphere are well known [25] and reported in section B.1.1. The external boundary conditions for the fluid flow are time dependent, namely $\boldsymbol{U}_{\boldsymbol{\partial\Gamma}} = \boldsymbol{U}(t) = \boldsymbol{U}(a(t))$. We will use for each time t the fluid flow that is instantaneously the stationary solution for the Stokes's equation satisfying the fluid boundary conditions. The boundary conditions for the nutrient concentration field, C are:

$$C(R,\theta) = 0, \qquad C(R_{ext},\theta) = 1, \tag{A.1}$$

where R is the organism radius and R_{ext} is the external boundary that should satisfy $R_{ext} \gg R$ in order to represent the condition $R_{ext} \to \infty$. The axi-symmetry, present in the fluid flow and in the concentration boundary conditions, allows, after a passage of the equation 1.11 in cylindrical coor-

dinates, to perform 2-D instead of 3-D simulations (see section A.1 for the equations solved and for the code). We performed part of the simulations using the commercial software COMSOL Multiphysics R V5.2 [108] and part of the simulations using the free software Freefem++ [109], where both of these programs use finite elements to solve the equations. The mesh grid is constructed in order to produce a difference between the computed uptake and the analytic prediction in the case $Pe = 0$ of the order of 10^{-3}. The external boundary is a sphere of radius $R_{ext} = 10^4 r$. The difference in the uptake between the analytic solutions with $R_{ext} \to \infty$ and $R_{ext} = 10^4 r$ is of the order 10^{-4}, therefore less than the numerical error, see supplementary information section B.1.3. We maintained the step time dt always lower than $0.01/A$. We define two quantities: the integral absolute variation in the concentration field at each time step, e.g. $\Delta C(dt) = \int_\Gamma |C(\boldsymbol{X}, t+dt) - C(\boldsymbol{X}, t)| d\boldsymbol{X}$, where Γ is the volume inside the boundaries and the total absolute possible variation in the concentration field defined as $\Delta C_T \int_\Gamma |C(\boldsymbol{X}; a_1) - C(\boldsymbol{X}; a_2)| d\boldsymbol{X}$, where $C(\boldsymbol{X}; a_1)$ and $(\boldsymbol{X}; a_2)$ denotes the stationary solution for the concentration field with a flow respectively $U(a_1)$ and $U(a_2)$. The parameter a_1 and a_2 will be defined later, but they are also representative of the maximum and minimum values, during each simulation, of the parameter a. This quantities are used as parameters in order to ensure enough precision at every step, maintaining dt so that $\Delta C(dt) < 6.e^{-3} C_T$.

A.1 Numerical methods

A.1.1 Diffusion equation

The stationary diffusion equation is

$$\nabla^2 C = 0 \tag{A.2}$$

that in cylidrical coordinate is

$$\frac{1}{r}\partial_r r\partial_r C + \partial^2_{zz} C = 0$$

where we consider $\partial_\theta C = 0$ due to axial symmetry. Multiplying by r,

$$\partial_r r\partial_r C + \partial_z r\partial_z C = 0$$

and for a test function T, we obtain:

$$T\partial_r r\partial_r C + T\partial_z r\partial_z C = 0.$$

Integrating over the volume and than proceeding with an integration by parts we obtain:

$$\int_\Gamma r((\partial_r T)(\partial_r C) + (\partial_z T)(\partial_z C)) + \int_{\partial\Gamma} rT((\partial_r c)n_r + (\partial_z C)n_z) = 0$$

where Γ is the domain of integration, $\partial\Gamma$ the external boundaries and n_r, n_z are the $\hat{\boldsymbol{r}}$ and $\hat{\boldsymbol{z}}$ components of the normal to the exterior boundary.

A.1.2 Advection-diffusion equation

Starting from eq. 1.11 and proceeding as for the diffusion equation we can come to

$$\int_\Gamma rT\partial_t C + \int_\Gamma rT(U_z\partial_t C + U_r\partial_t C)D \int_\Gamma r((\partial_r T)(\partial_r C) + (\partial_z T)(\partial_z C)) + \int_{\partial\Gamma} rT((\partial_r c)n_r + (\partial_z C)n_z) = 0. \tag{A.3}$$

A.2 Code

The advection part of equation A.3 is solved by the standard convection operator present in FreeFem++ called CONVECT that use Characteristics-Galerkin Method

```
problem DYNCAX( C, T, eps=-1.0e-9 ) =
  - int2d ( Th ) ( (C) * T / dt*x ) +int2d ( Th ) ( (Cold) * T / dt*x )
```

```
  + int2d ( Th ) ( -(u1*dx(C)*T +u2*dy(C)*T )*x )
  + int2d ( Th ) ( Diff*(  dx ( C ) * dx ( T ) +   dy ( C ) * dy ( T )
)*x )
  + int1d(Th,IntS) (Diff*x*T* ( dx(Cold)*N.x+dy(Cold)*N.y ))
  + int1d(Th,ExtS) (Diff*x*T* ( dx(Cold)*N.x+dy(Cold)*N.y ))
  + on(ExtS,  C=1.0 )
  + on(IntS, C=0.0 );
```

where X and Y stands for r and z in equation A.3, and COLD is $C(t - dt)$. EXTS is the external border while INTS is the internal border. Since the matrix E is invariant for z reversal, we solved the equations A.3 only in the first quadrant. The mesh generated has 589610 triangles, and 296366 vertices.

A.3 Results

A.3.1 Transient time

As a first step we want to analyze the transient time in the nutrient uptake when a sudden change in the fluid flow occurs. Hence, we will consider a fluid flow that passes from $U(a_1)$ to $U(a_2)$ at time $t = 0$, and a concentration field that for $t < 0$ is the stationary solution obtained with a stationary $U = U(a_1)$. Then, we record the transient instantaneous uptake $F(t)$. A selection of results with different a_1 and a_2 is plotted in figure A.5, in which is possible to note a dependency of the transient time in the nutrient uptake on both $|a_1|$ and $|a_2|$. In order to proceed with clarity, we will start by showing the results for two particular cases: $a_2 = 0$ and $a_1 = 0$ and afterwards proceed to the general case. In the simple case of $a_2 = 0$, we have to solve the transient time of the diffusion equation initialized with a non equilibrium

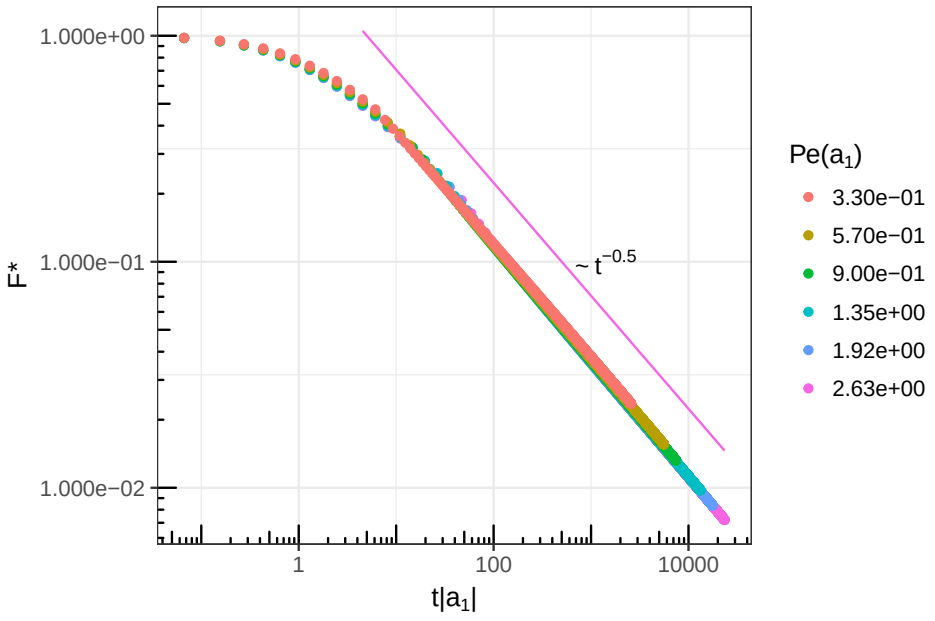

Figure A.1: Log-Log plot of $F*$ against the dimensionless time $t\ a_1$ for different values of a_1 and with $a_2 = 0$. As is possible to see all the curves collapse and the re-scaled flux decay as a power law with exponent -1/2 .

solution. We define F^*, the adimensionsional re-scaled uptake, as

$$F^*(t) = \frac{F(t) - F(a_1)}{F(a_2) - F(a_1)} \tag{A.4}$$

where $F(t)$ is the instantaneous uptake at time t and, $F(a_2)$ and $F(a_1)$ are the stationary uptake for, respectively, $U = U(a_1)$ and $U = U(a_2)$. In figure A.1, we show the log-log plot of F^*, plotted against the dimensionless time $t\ a_1$. All the curves of the re-scaled flux F^* collapse into a single curve, which for $t \gg 1/a_1$ is well fitted with a power law with exponent -1/2.

In the case $a_1 = 0$, the concentration field is instead initialized with the stationary solution of the diffusion equation and, for $t > 0$, the fluid flow is turned on with $U = U(a_2)$. This case is qualitatively different from the previous one: the uptake converges to the asymptotic value in a finite time,

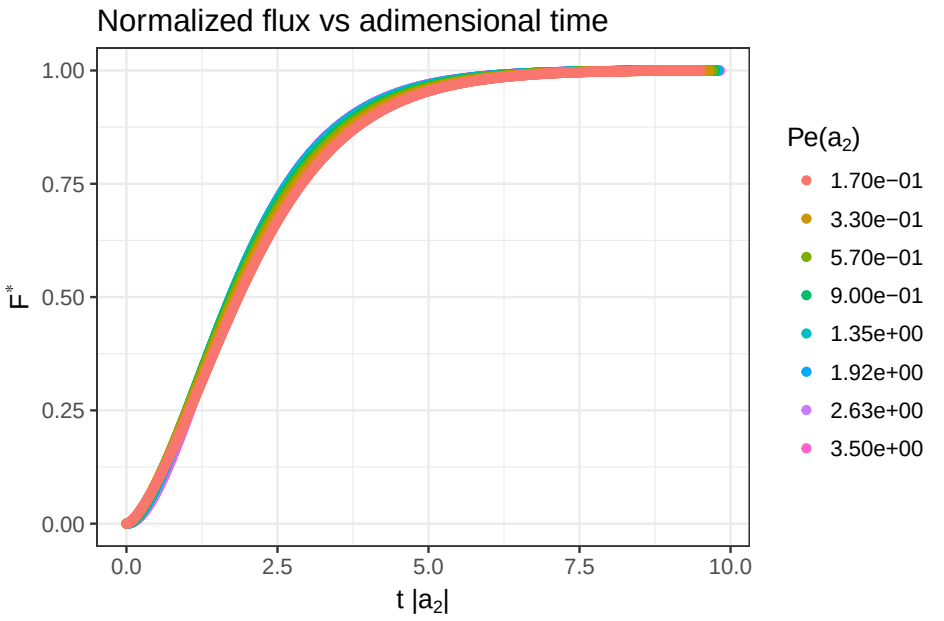

Figure A.2: Linear plot of the normalized flux against the dimensionless time always starting from the stationary solution with $a_1 = 0$ for different value of a_2. As is possible to see all the curves collapse and differently from the case of only diffusion the asymptotic flux is reached in a finite time.

namely exponentially. The transient time scales with a_2, as it can be seen in figure A.2, in which we plot the re-scaled flux F^* against the adimensional time ta_2. As we can see, all the curves collapse into a single curve.

By taking into account all the possible values of a_1 and a_2, the results can be classified with regards to the following possibilities: if a_1 is of the same sign of a_2, and, if this is the case, if $a_1/a_2 < 1$. The cases in which a_1 has the same sign of a_2 and $a_1/a_2 < 1$ brings, as seen also for the case $a_1 = 0$, to a finite transient time in the uptake. The transient time scales mostly with a_2 and with a small dependence on a_2/a_1. In figure A.4 we show the collapse of all the curves, if plotted against to a dimensionless time obtained as $t/a_2\ (1 + \alpha(a_1/a_2)^\beta)$. The parameters α and β are obtained by

a non-linear fit, using as variables the inflection point time of every curve against the parameters a_1 and a_2. The fitted values are $\alpha = 1.4 \pm 0.2$ and $\beta = 0.26 \pm 0.07$. The small fitted value of β is indicative of a lower dependence of the transient time on a_1 respect to a_2 . The cases in which a_1 has the same sign of a_2 and $a_2/a_1 < 1$ instead F^* can be well fitted for $t \gg 1/a_1$ by an exponentially truncated power law as $(ta_1)^{-0.5}e^{-ta_2}$. A representative log-log plot of F^* versus ta_1 and the proposed fitting function for $a_1/a_2 = 100$ is shown in figure A.3.

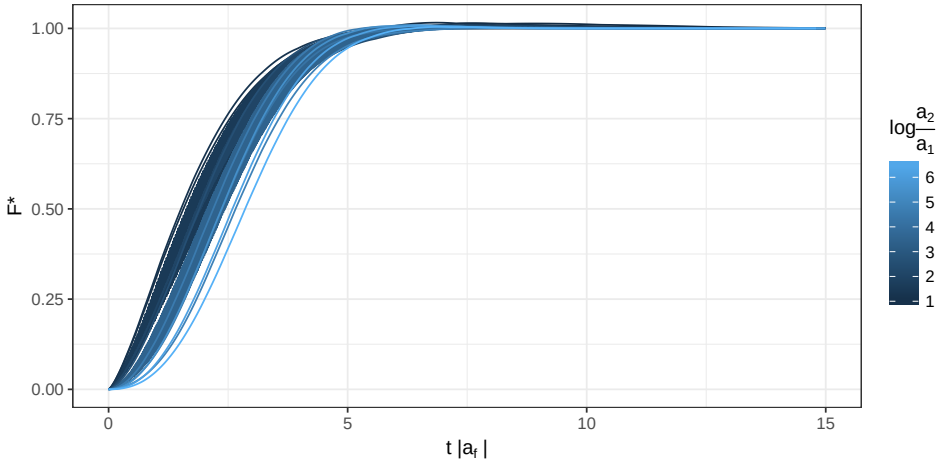

Figure A.4: Plot of the re-scaled uptake F^* versus the dimensionless time t/a_f, where $a_f = a_2(1 + \alpha(a_1/a_2)^\beta)$, for different values of a_1 and a_2 with $a_1, a_2 < 0$ and $|a_1|/|a_2| < 1$. As is possible to see by visual inspection the collapse can be refined.

Changing sign from a_1 to a_2, where the most simple case is $a_2 = -a_1$, result in a transient uptake where is present a time interval in which $F(t) < \min(F(a_2), F(a_1))$. There is no surprise in this since is well known that rotations and so oscillations reduce the mean flux in the fluid flow [110].

For completeness we present in figure A.5 the plot of the uptake versus time for different values of a_1 and a_2.

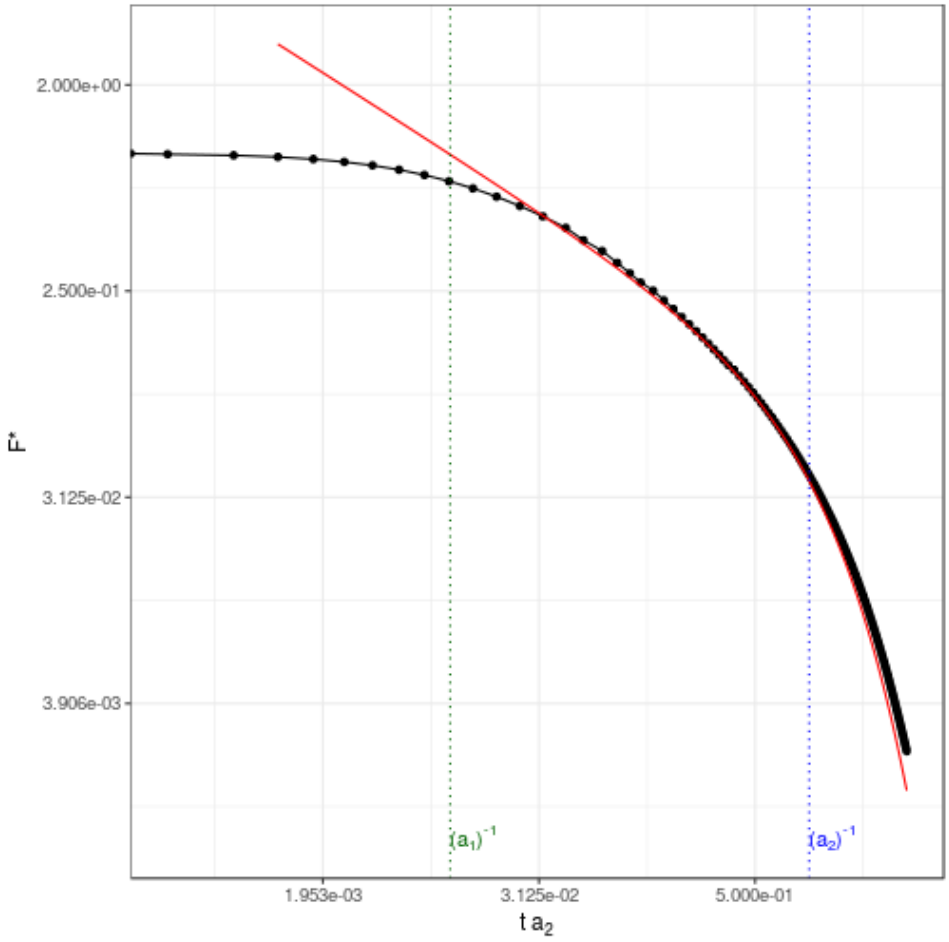

Figure A.3: Log-log plot of $F*$ for the case $a_1 = 100a_2$. The two time scale $(a_1)^{-1}$ and $(a_2)^{-1}$ are showed in dotted. In red is plotted the function $(ta_1)^{-0.5}e^{-ta_2}$ that well describe the flux for $t \gg (a_1)^{-1}$.

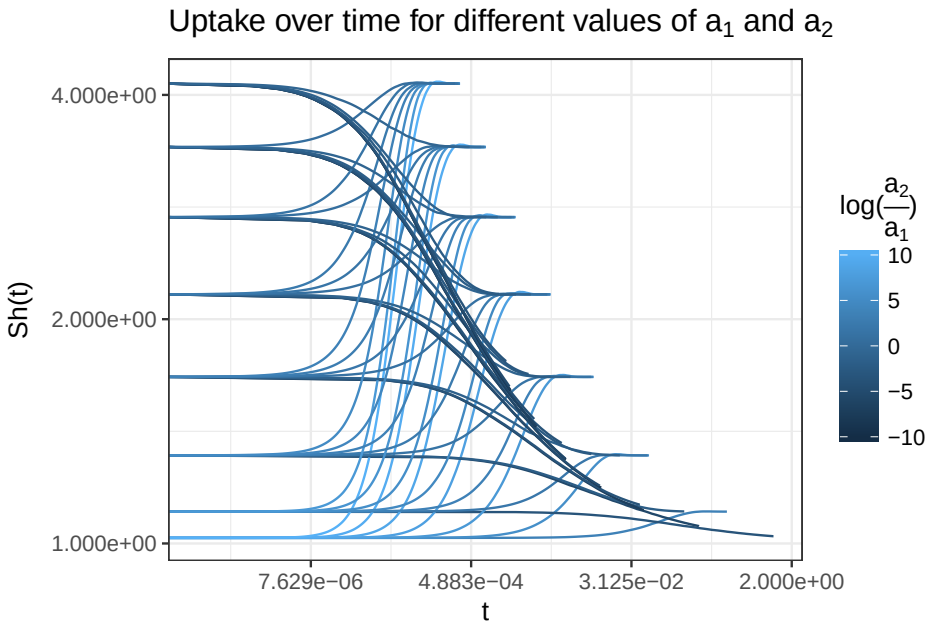

Figure A.5: Log-Log plot of the uptake versus time for different values of a_1 and a_2, all with $a_1, a_2 < 0$. As is possible to see the transient time for $a_2/a_1 > 1$ is faster than if $a_2/a_1 < 1$. Also the transient time seems to depend strongly on a_2.

A.3.2 Time dependent flow: Enhanced uptake

Due to the previous results we might expect that we can construct some periodic flow with a mean uptake greater than the uptake of the mean flow. In order to demonstrate this assumption, we perform a simple numerical experiment: we switch between two static flows every time interval ΔT with different values of a, that we will call again a_1 and a_2. We use as initial concentration field the stationary solution of the advection-diffusion equation with $a = (a_1 + a_2)/2$ and, in order to achieve the asymptotic periodic cycle for the uptake, each simulation lasts for the max between $10\Delta T$ and $10/\max(a_1, a_2)$. A subset of exemplary results are shown in Figure A.6 where is plotted the instantaneous uptake respect to time for different values of ΔT

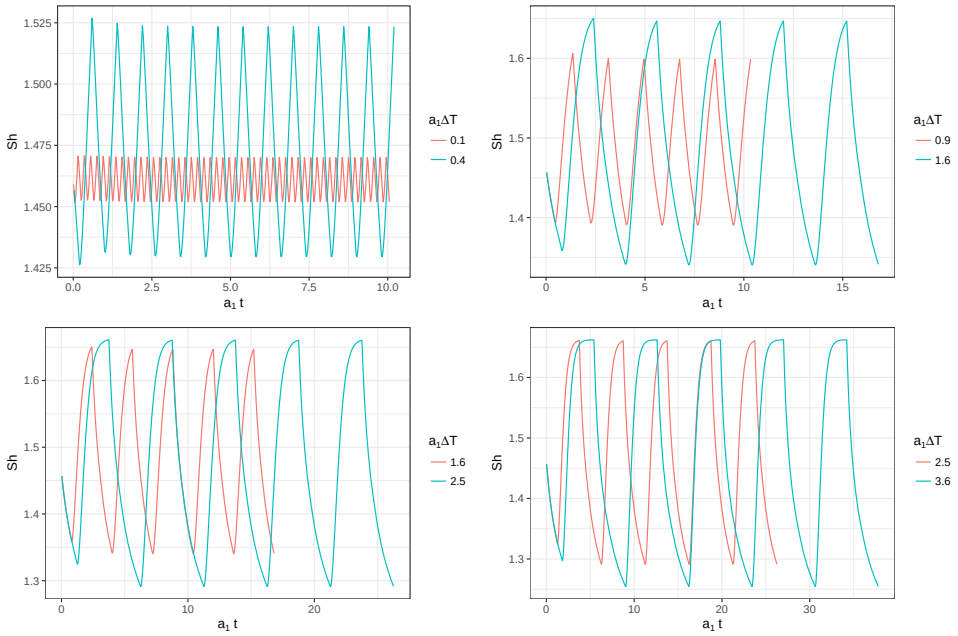

Figure A.6: Example of the nutrient uptake in time for different value of $\Delta T a_1$ with $Pe(a_1) \sim 2.63$ and $a_2 = 0/s$. Each simulation last for the max between $10\Delta T$ and $10/a_1$, in order to be sure to achieve the asymptotic periodic cycle for the flux. As it is possible to see the flux reach the asymptotic value for $\Delta T \sim 1/a_1$. The concentration field is initialized with the static solution with $a = (a_1 + a_2)/2$.

and $Pe(a_1) \sim 2.63$ and $Pe(a_2) = 0$.

In figure A.8 we plot the dependence of the asymptotic mean uptake, for different values of a_1 and with $a_2 = 0./s$. In order to see better the variation respect to the expected values we plot the normalized variation respect to $F((a_1 + a_2)/2)$. As it is possible to see, the average uptake has a maximum for $\Delta T \sim 1/a_1$ with a peak value that is greater than $F((a_1 + a_2)/2)$. Instead, for $\Delta T << 1/a_1$ and $\Delta T >> 1/a_1$, the average value is lower than $F((a_1 + a_2)/2)$. This effect is quite relevant since in turbulence one of the time scales of the matrix A is expected to be of the order of $1/\sqrt{A_{ij}A_{ij}}$. By inverting the sign of a_1 the shown above result holds: in the

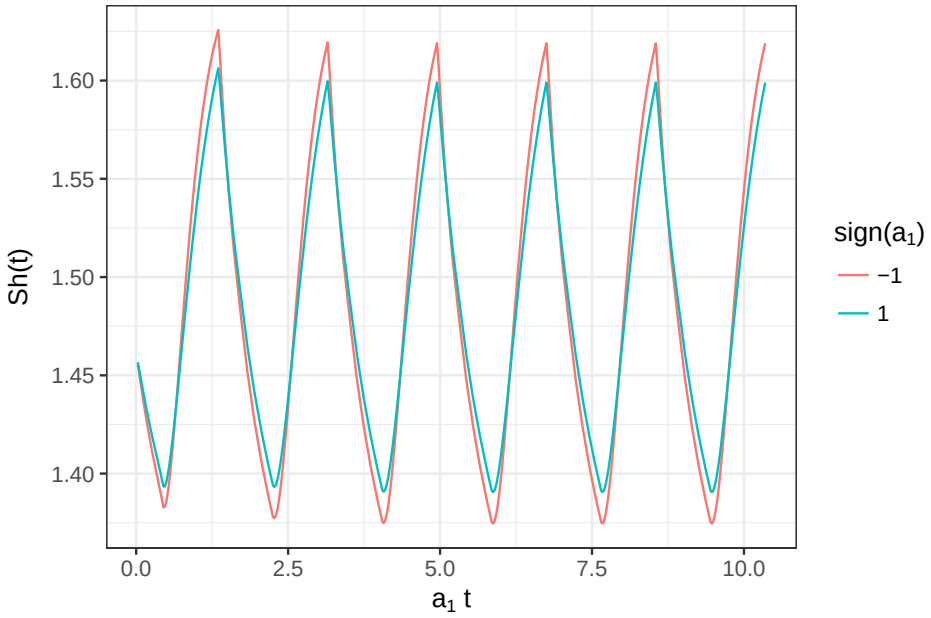

Figure A.7: Flux with $\Delta T = 0.9/|a_1|$ for $Pe(a_1) \sim 2.63$ and $a_2 = 0$. As it is possible to see the difference of sign change the time scale slightly for both the advective and diffusive part. As it is possible to see in figure A.8 the difference of uptake averaged on a period is largely under the error of measure.

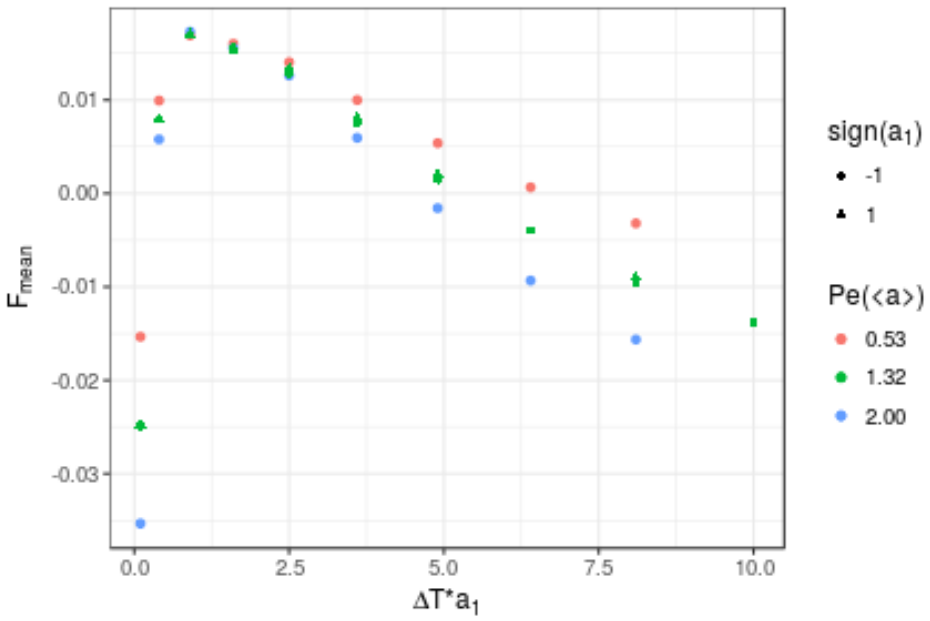

Figure A.8: Plot of F_{mean}, the normalized variation of the mean flux respect to the stationary uptake using the mean a, so $\frac{<F(a)>-F(<a>)}{F(<a>)}$ for different dimensionless time periods. The calculation of $< F(a) >$ is performed calculating the mean of the flux over the last 3 periods (so $6\Delta T$). We use a simple trapezoidal rule (Simpson rule has a difference of less than 1e-5). Three different possibles values of a_1 are used, and in legend is reported the equivalent Pe for a stationary flow with $a = (a_1 + a_2)/2$. As is possible to see there is a peak for $a_1 \Delta T \sim 1$.

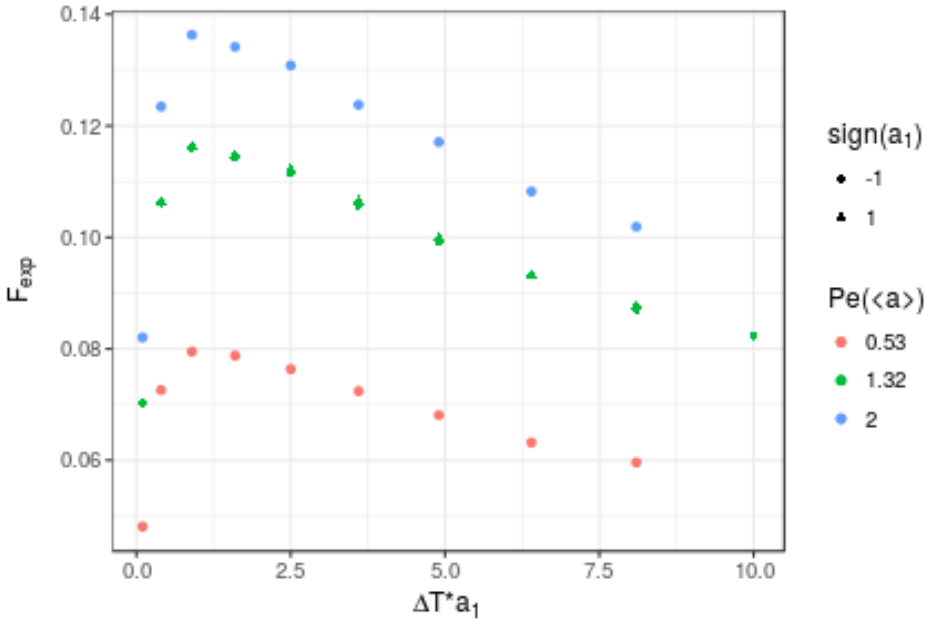

Figure A.9: Plot of F_{exp}, the normalized variation of the mean uptake respect to the expected average uptake: $\frac{<F(a)>-(F(a_1)+F(a_2))/2}{(F(a_1)+F(a_2))/2}$ for different dimensionless period times. As it can be seen the variation growth with $Pe(<a>)$ and it can be significative already for small values of $Pe(<a>)$.

range of parameters considered, the measured differences in the mean flux are in the range of error. In figure A.10 we plot the normalized variation respect to $(F(a_1)+F(a_2))/2$ and since $(F(a_1)+F(a_2))/2 \leq F\left((a_1+a_2)/2\right)$ the variation is greater than 10%.

If instead a_2 has a different sign respect to a_1 the average uptake is always lower than $F((|a_2|+|a_1|)/2)$. If $a_2 = -a_2$, for $\Delta T \ll 1/|a_1|$ the mean Sherwood number is heavily depressed on 1 as expected by previous numerical results for oscillatory flows [110], and by analogy with the classical results of [20] when $|\Omega|/|E| \gg 1$ with Ω being the anti-symmetric part of the gradient tensor A.

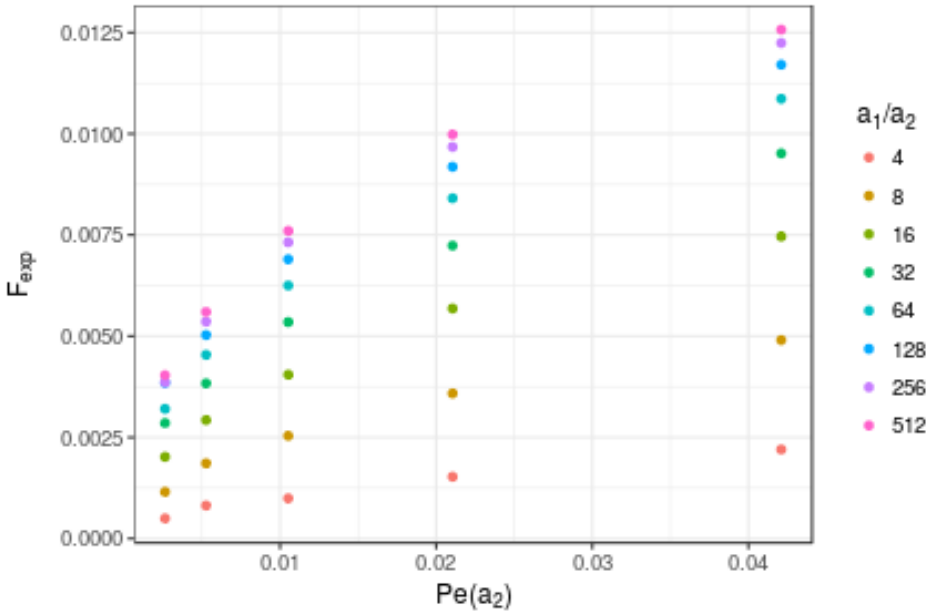

Figure A.10: Plot of F_{exp}, the normalized variation of the mean uptake respect to the expected average uptake: $\frac{<F(a)>-(F(a_1)+F(a_2))/2}{(F(a_1)+F(a_2))/2}$ for different dimensionless period times. As it can be seen the variation growth with $Pe(< a >)$ and it can be significative already for small values of $Pe(< a >)$.

A.3.3 Conclusion

We have clearly demonstrated the importance of the temporal correlations of the fluid flow in the nutrient uptake. The transient times of the nutrient flux toward a small organism are not symmetric inverting a_1 with a_2. As a result the average nutrient uptake is dependent on the flow time dynamics, and can be greater than the stationary flux characterized by the same mean Peclet number. These results open to more in depth investigations on the nutrient uptake of micro-organisms in turbulent flows, since the more relevant positive corrections to the mean uptake should occur when the duration of the gradients in the flows, namely a in our model, is close to $1/a$ as in turbulent flows. We want to stress that micro-organisms use the nutrient uptake to increase their volume, and so their linear dimension. Therefore, large positive fluctuations in the uptake lead to an increase in the Pe number, providing a positive feedback in the correlation between fluctuations in the gradient matrix and the growth rate.

Appendix B

Miscellaneous

B.1 Microscale

B.1.1 Velocity field near a sphere

The velocity field near a sphere is:

$$u = E \cdot x \left(1 - \frac{a^5}{r^5}\right) + \frac{1}{2}(\omega \wedge x)(1 - \frac{a^3}{r^3}) - \frac{5}{2}x(x \cdot E \cdot x)\left(\frac{a^3}{r^5} - \frac{a^5}{r^7}\right) \quad \text{(B.1)}$$

B.1.2 Orientation

The orientations of a prolate ellipsoid in a linear general flow it is an old result by Jeffery [111] that can be recast as:

$$\frac{d\boldsymbol{v}}{dt} = \boldsymbol{\Omega v} + \gamma\left(\boldsymbol{Ev} - \boldsymbol{v}(\boldsymbol{vEv})\right), \quad \text{(B.2)}$$

where $\boldsymbol{v}$ is the versor of the long axis of the ellipsoid and $\gamma = \frac{1-\beta^2}{1+\beta^2}$ is a parameter that take in account the aspect ratio of the ellipsoid $\beta = a/c$ with a being the short axis and c the long axis. The parameter γ is bounded to be between 0 in case of sphere and tend to 1 for $\beta \to 0$. We simulated a synthetic turbulent matrix using the algorithm described in [112]. This algorithm mimic the pdf of the gradient matrix A in turbulence as well its geometrical properties and is characterized by two time scales T_c, the

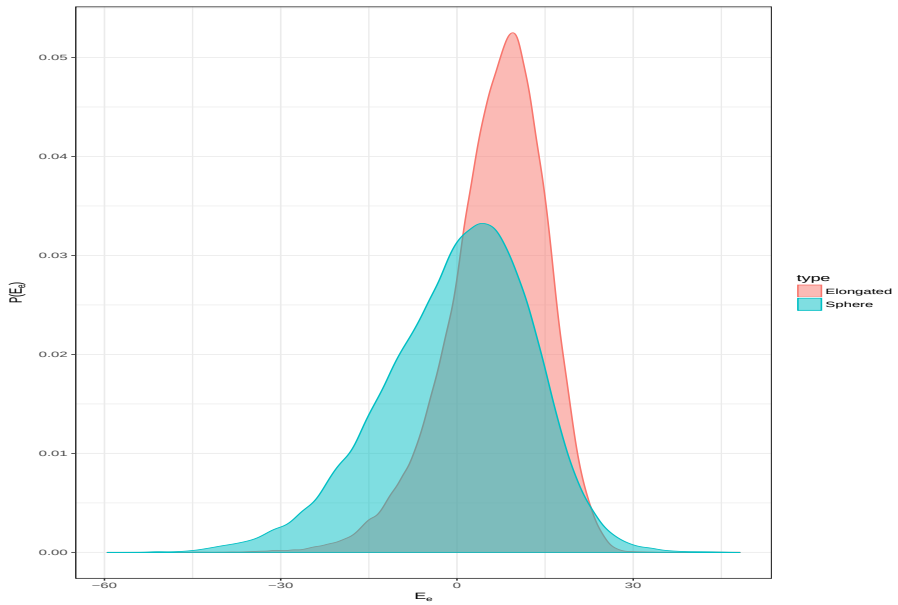

Figure B.1: Pdf of the projection of the shear tensor on a random initial axis for a sphere and on the longer axis for an ellipsoid. The mean of the pdf for the sphere is 0, while for the ellipsoid is different from 0.

integral time scale and the Kolmogorov time scale $\tau_\eta = \left(\frac{\nu}{\varepsilon}\right)^{1/2}$. Then we follow the orientation of 5 particles with different values of γ respectively $(0, 1/2, 2/3, 4/5, 9/10)$, using eq B.2. In particular we followed the dynamics of the versor of the longest axis of the prolate ellipsoid and of a initial random direction for the spherical case, and collect the projections of the matrix on these versors, mean $v_i E(i,j) v_j$. We discover that the elongation has a deep influence both on the pdf of the projection and the auto-correlation time of the projection. The pdf of the projection passes from being with 0 mean in the spherical case, to a non zero mean in all other cases (see Figure B.1) while the auto-correlation time of the projection increases with the elongation (see Figures B.2).

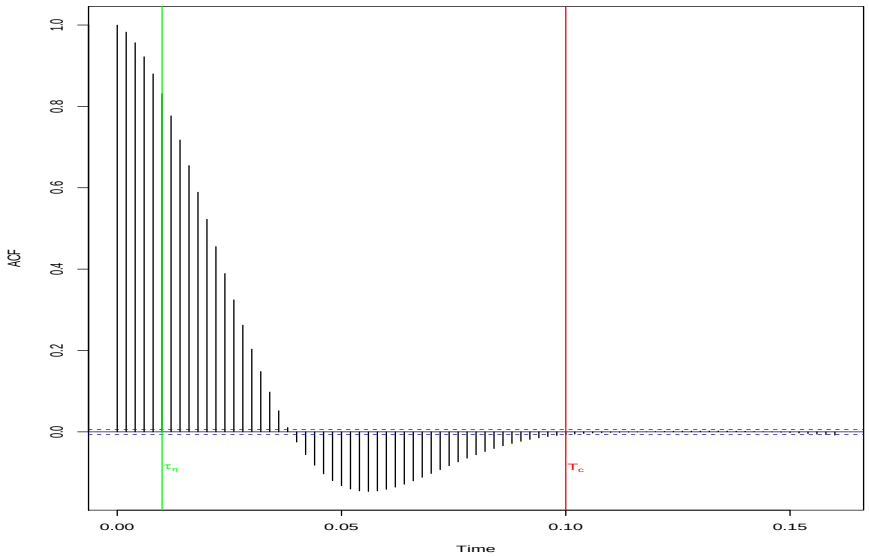

(a) Sphere.

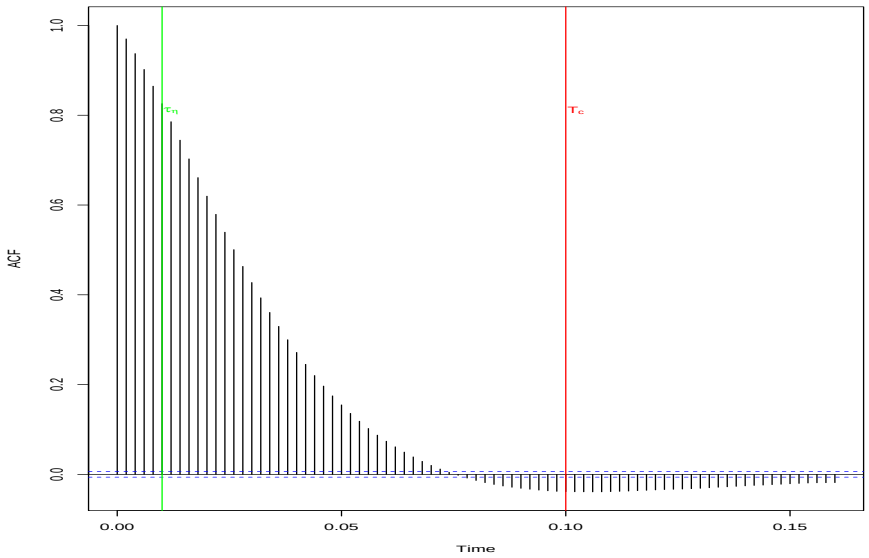

(b) Ellipsoid.

Figure B.2: Autocorrelation function for the projection of the shear tensor on a random initial axis for a sphere and on the longer axis for an ellipsoid.

B.1.3 Analytical solution for uptake of a sphere in quiescent fluids

Using the Laplacian in 3 dimensions the diffusion equation can be rewritten as:

$$\frac{D}{r^2}\partial_r r^2 \partial_r C = 0 \tag{B.3}$$

From simple calculations and imposing the boundary conditions as defined in equations A.1 the analytic solution of the nutrient concentration is:

$$C(r) = \frac{R_{ext}}{R_{ext} - R} - \frac{R_{ext} R}{(R_{ext} - R) r} \tag{B.4}$$

Since the flux is proportional to $\partial_r C(R)$, the analytical ratio in the uptake between an external boundary at a finite distance and the limit $R_{ext} \to \infty$ goes as $\frac{R_{ext}}{(R_{ext}-R)}$ that in case $R_{ext} = 10^4 R$ values only 1.0001

B.1.4 Extension for low Re

The relationship $\sigma^2_{\ln \epsilon} = A + (3\mu/2)\ln(R_\lambda)$ clearly lost sense when predict $\sigma^2_{\ln \epsilon} < 0$. Supposing that a relationship of the kind $A + \frac{R_\lambda^{2/3}}{R_\lambda^{2/3}+k} \cdot 0.25 \cdot 1.5 \log(R_\lambda^{2/3})$ and extimating k using the data in [6] we obtain $k = 83$.

B.1.5 Comparison with an ellipsoid

Since many authors approximate the E.Coli with an ellipsoid of revolution we recast the known formula for it in order to compare the results. If we will call b the length of longest semi-axis of the prolate ellipsoid and c the length of the two smallest semi-axis, and the ratio between the the semi-axis $\chi = c/b < 1$.

We remind the definition of the eccentricity and the formula for the dimensional surface of the ellipsoid:

$$e = \left(1 - \chi^2\right), \qquad S = 2\pi c^2 \left(1 + \frac{b}{ce} \cdot \arcsin(e)\right)$$

In [113] is presented a general formula for Sh_0 of a prolate ellipsoid $Sh_0 = Sh_0(c,d)$

$$Sh_0(c,b) = 2\sqrt{\pi}c/\sqrt{S}\sqrt{\frac{1}{\chi^2}-1}\left[\log\left(\frac{1}{\chi}+\sqrt{\frac{1}{\chi^2}-1}\right)\right]^{-1} \tag{B.5}$$

In [114] is presented a formula for extrapolate the Sherwood number for all Pe numbers and all χ:

$$\mathrm{Sh} = \frac{0.5\ \Pi}{Sa_e} + \frac{1}{S}\left(0.125\left(\frac{\Pi}{a_e}\right)^3 + (7.85K[\chi])^3\mathrm{Pe}\right)^{1/3} \tag{B.6}$$

where

$$K(\chi) = \left(\frac{4}{3}\right)^{1/3}\chi^{-2/9}(1-\chi^2)^{1/3}\left(\frac{(2-\chi^2)}{2\sqrt{1-\chi^2}}\log\left(\frac{1+\sqrt{1-\chi^2}}{1-\sqrt{1-\chi^2}}\right)-1\right)^{-1/3}$$

and S is the adimensional surface area[1] defined as S^*/a_e^2 and Π is the conductance (or shape factor), defined as:

$\Pi = \frac{\alpha S}{D}$ where α is the mass-transfer coefficient defined as $\alpha = \frac{Q}{S^* C_\infty}$ In [113] is presented a general formula for the conductance of a prolate ellipsoid $\Pi = \Pi(a,b)$

$$\Pi(a,b) = 4\pi a\sqrt{\frac{1}{\chi^2}-1}\left[\log\left(\frac{1}{\chi}+\sqrt{\frac{1}{\chi^2}-1}\right)\right]^{-1}$$

B.1.6 Numerical values for the fits of the fluxes

Assuming a fixed value of R, that in our case of study is $R = 0.4\mu m$, the characteristic length is $le(h)$ is equal to $((2R(h/2-R)+4R^2)/4)^{0.5}$. Using the definition we gave of Pe_1, the Peclet number referring to le it is $Pe(le) = (le(h))^2 Pe_1$. The equation fitted for the uptake in still water is:

$$h'(t) = (1 + 1.26(h(t))^{0.8}), \qquad h(0) = \Delta \tag{B.7}$$

[1] $$S = S^*/a_e^2 = \frac{2\pi}{\chi^{1/3}}\left(\chi + \frac{1}{e}\cdot\arcsin(e)\right)$$

While in case of $Pe > 0$, using the 3 functions obtained from the previous fits:

$$\begin{aligned} K1(le) &= -0.9316 + 2.3030(le(h)); \\ K2(le) &= 1.7141 - 0.5647(le(h))^{-1.1372}; \\ K3(le) &= 1.0737 - 0.5052(le(h)); \end{aligned} \tag{B.8}$$

the equation for the evolution of h is:

$$h'(t) = (1 + 1.26(h(t))^{0.8}) \left(0.5 + (0.125 + 0.27K1(le) \left(Pe(le)^{0.5K2(le)} + K3(le)0.9^3(Pe(le))\right)^{1/3}\right) \times (1 + 0.01(Pe(le))/(0.001 + (Pe(le)) \tag{B.9}$$

Where le is obviously $le = le(h(t))$.

B.2 Macroscale

B.2.1 Power-laws with double-exponential truncation are a robust defining characteristic of olfactory-cued navigation

[89] obtained an analytic expression of the step-length distribution by assuming that odor concentrations were exponentially distributed. The assumption is broadly consistent with observations of odor concentrations and our predictions provide good fits to the shearwater flight pattern data. Their key prediction is the occurrence of doubly-exponentially truncated 3/2 power-laws which [89] took to be the hallmark of olfactory-cued navigation. Here we provide evidence that this defining characteristic is not specific to the model of [89] but instead arises generally from physically realistic models of olfactory-cued navigation.

To do this we have calculated the step-length under the assumption that odour concentrations are Gaussian distributed rather than exponentially distributed. This assumption is not very realistic but that does not matter

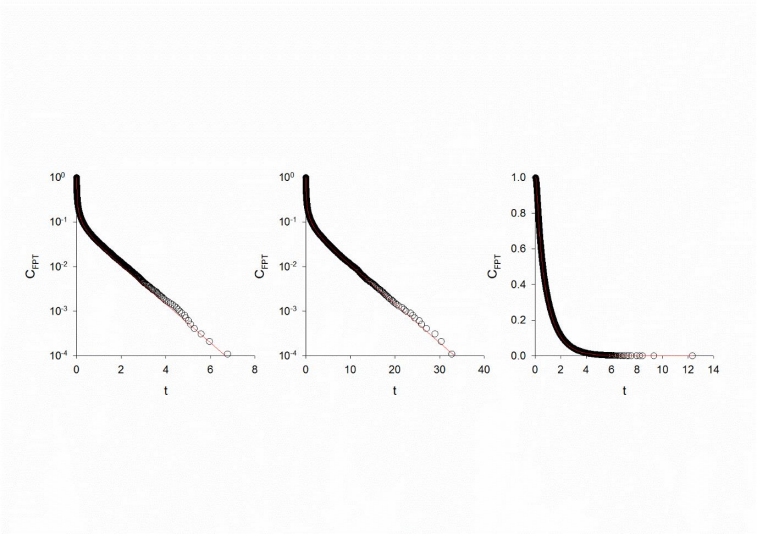

Figure B.3: Figure Comparison of simulation data (o) and theoretical predictions (red lines) for a variety of parameter values showing that the theory works.

because the goal here is to test the robustness of doubly-exponentially step-length distributions with respect to modeling assumptions. The calculation is long and tedious but mirror closely that of [115]. The end result can be expressed most succinctly as

$$C = Rank.Freq.Distr. = erf\left(\frac{c_0 e^{-t/T}}{\sqrt{2(1-e^{-2t/T})}\sigma_c}\right) \tag{B.10}$$

where for simplicity the detection threshold $c_T = 0$. It follows that the step-length (step-duration) distribution, $p = \frac{-\partial C}{\partial t}$, is given by

$$p(t) = \frac{c_0}{\pi\sigma_c}\frac{T^{1/2}}{t^{3/2}}e^{-c_0^2 T/(8\sigma_c^2 t)} \tag{B.11}$$

for long times. And so once again we have doubly-exponentially truncated 3/2 power-laws. This suggests that double-exponentially truncated 3/2 power-laws are a robust prediction that arises independently of modeling assumptions about how odours are distributed. As in the shearwater paper $\lambda_1 \propto 1/T$,and $\lambda_2 \propto T c_0^2$.

B.2.2 Mechanistic wind effects on trajectories

In principle the observed correlations between λ_1 and λ_2 and the wind speed could be originated mechanistically by the impact of wind on the movement of birds [103]. In particular we could expect that head-wind could reduce and tail wind could impact sistematically both the cut off values (namelly increasing λ_2 and decreasing λ_1). We have no specific predictions for cross winds. To test for this effect, for each bird we computed the average projection of the wind on the movement direction ($< v^{\parallel} >$) and evaluated how much this variable could explain the value of the cut offs. If the value of the cut offs is only determined by the mechanistic effect of wind we should find a significative effect and a model with both wind speed and $< v^{\parallel} >$ should outperform the models reported in figure 3 and 4 of the main text. Inverselly, a non significant $< v^{\parallel} >$ correlation mean that the mechanistic effect of wind direction is not very relevant.

For all possible days of travel subsets we have two cases: or the best aic is found using the model with only the mean wind, selecting so our model, or the best aic is found using $\log(< v >)$ and $< v^{\parallel} >$, but still the significance and the standardized coefficient of the term $< v^{\parallel} >$ is poor compared to the one of $< v >$, meaning that a mechanicistic effect of the wind if present, is much less relevant than the olfactory navigation in determining the values of both λ_1 and λ_2. Regarding λ_1, subsetting the dataset for travels that last more than four days (subset where there is the greatest advantage for the alternative model among all the subsets) we have a Δ AIC of -1.3 for the model $\lambda_1 \sim \log(< v >) + < v^{\parallel} >$, but the ratio of the coefficients of the glm between $\log(< v >)$ and $< v^{\parallel} >$ is 2.5 and the p.values of $\log(< v >)$ and $< v^{\parallel} >$ is respectively: $p < 0.0001$ and $p = 0.018$.

Regarding λ_2 sub-setting the data-set for travels that last more than four days, the Δ AIC is 1.99 and the model should be rejected.

Bibliography

[1] U Frisch, T Matsumoto, and J Bec. "Singularities of Euler flow? Not out of the blue!" In: *Journal of Statistical Physics* 113.5 (2003), pp. 761–781.

[2] Edward M Purcell. "Life at low Reynolds number". In: *American journal of physics* 45.1 (1977), pp. 3–11.

[3] Eric Lauga et al. "Swimming in circles: motion of bacteria near solid boundaries". In: *Biophysical journal* 90.2 (2006), pp. 400–412.

[4] Sangtae Kim. "Singularity solutions for ellipsoids in low-Reynolds-number flows: with applications to the calculation of hydrodynamic interactions in suspensions of ellipsoids". In: *International journal of multiphase flow* 12.3 (1986), pp. 469–491.

[5] URL: `http://glossary.ametsoc.org/wiki/Kolmogorov%27s_similarity_hypotheses` (visited on 11/13/2017).

[6] PK Yeung et al. "Acceleration and dissipation statistics of numerically simulated isotropic turbulence". In: *Physics of fluids* 18.6 (2006), p. 065103.

[7] Andrey Nikolaevich Kolmogorov. "A refinement of previous hypotheses concerning the local structure of turbulence in a viscous incompressible fluid at high Reynolds number". In: *Journal of Fluid Mechanics* 13.1 (1962), pp. 82–85.

[8] ZOLTAN Neufeld and T Tél. "Advection in chaotically time-dependent open flows". In: *Physical Review E* 57.3 (1998), p. 2832.

[9] G. Falkovich, K. Gaw ędzki, and M. Vergassola. "Particles and fields in fluid turbulence". In: *Rev. Mod. Phys.* 73 (4 2001), pp. 913–975. DOI: 10.1103/RevModPhys.73.913. URL: http://link.aps.org/doi/10.1103/RevModPhys.73.913.

[10] Paul G Falkowski. "The role of phytoplankton photosynthesis in global biogeochemical cycles". In: *Photosynthesis research* 39.3 (1994), pp. 235–258.

[11] Amer Al-Homoud and Miki Hondzo. "Enhanced uptake of dissolved oxygen and glucose by Escherichia coli in a turbulent flow". In: *Applied microbiology and biotechnology* 79.4 (2008), pp. 643–655.

[12] Miki Hondzo and Alfred Wuest. "Do microscopic organisms feel turbulent flows?" In: *Environmental science & technology* 43.3 (2008), pp. 764–768.

[13] Jeffrey S Guasto, Roberto Rusconi, and Roman Stocker. "Fluid mechanics of planktonic microorganisms". In: *Annual Review of Fluid Mechanics* 44 (2012), pp. 373–400.

[14] Colin Torney and Zoltán Neufeld. "Transport and aggregation of self-propelled particles in fluid flows". In: *Physical review letters* 99.7 (2007), p. 078101.

[15] JT Locsei and TJ Pedley. "Run and tumble chemotaxis in a shear flow: the effect of temporal comparisons, persistence, rotational diffusion, and cell shape". In: *Bulletin of mathematical biology* 71.5 (2009), pp. 1089–1116.

[16] Howard C Berg. *E. coli in Motion*. Springer Science & Business Media, 2008.

[17] JAVIER JIMÉNEZ. "Oceanic turbulence at millimeter scales". In: *Oceanographic Literature Review* 3.45 (1998), p. 598.

[18] M Cencini et al. "Dynamics and statistics of heavy particles in turbulent flows". In: *Journal of Turbulence* 7 (2006), N36.

[19] Jeremie Bec et al. "Heavy particle concentration in turbulence at dissipative and inertial scales". In: *Physical review letters* 98.8 (2007), p. 084502.

[20] GK Batchelor. "Mass transfer from a particle suspended in fluid with a steady linear ambient velocity distribution". In: *Journal of Fluid Mechanics* 95.2 (1979), pp. 369–400.

[21] Andreas Acrivos. "A note on the rate of heat or mass transfer from a small particle freely suspended in a linear shear field". In: *Journal of Fluid Mechanics* 98.2 (1980), pp. 299–304.

[22] Chao Yang et al. "Mass/heat transfer from a neutrally buoyant sphere in simple shear flow at finite Reynolds and Peclet numbers". In: *AIChE Journal* 57.6 (2011), pp. 1419–1433.

[23] L Karp-Boss, E Boss, and PA Jumars. "Nutrient fluxes to planktonic osmotrophs in the presence of fluid motion". In: *Oceanographic Literature Review* 5.44 (1997), p. 530.

[24] L. Seuront. *Fractals and Multifractals in Ecology and Aquatic Science*. CRC Press, 2009. ISBN: 9781420004243. URL: `https://books.google.it/books?id=Far9Bfbw\_J8C`.

[25] L Gary Leal. *Advanced transport phenomena: fluid mechanics and convective transport processes*. Cambridge University Press, 2007.

[26] I.P. Gupalo, I.S. Riazantsev, and V.I. Ulin. "Diffusion on a particle in a homogeneous translational-shear flow". In: *Prikladnaia Matematika i Mekhanika* 39 (1975), pp. 497–504.

[27] Sattar Taheri-Araghi et al. “Cell-size control and homeostasis in bacteria”. In: *Current Biology* 25.3 (2015), pp. 385–391.

[28] Anastassia M Makarieva, Victor G Gorshkov, and Bai-Lian Li. “Energetics of the smallest: do bacteria breathe at the same rate as whales?” In: *Proceedings of the Royal Society of London B: Biological Sciences* 272.1577 (2005), pp. 2219–2224.

[29] Wikipedia contributors. *Renewal theory — Wikipedia, The Free Encyclopedia*. [Online; accessed 27-January-2018]. 2017. URL: `https://en.wikipedia.org/w/index.php?title=Renewal_theory&oldid=810230743`.

[30] Amer Al-Homoud and Miki Hondzo. “Energy dissipation estimates in oscillating grid setup: LDV and PIV measurements”. In: *Environmental Fluid Mechanics* 7.2 (2007), pp. 143–158.

[31] Òscar Guadayol et al. “Evaluation of oscillating grids and orbital shakers as means to generate isotropic and homogeneous small-scale turbulence in laboratory enclosures commonly used in plankton studies”. In: *Limnology and Oceanography: Methods* 7.4 (2009), pp. 287–303.

[32] Daniel B Blum et al. “Effects of nonuniversal large scales on conditional structure functions in turbulence”. In: *Physics of Fluids* 22.1 (2010), p. 015107.

[33] Caijuan Zhan et al. “Accumulation of motile elongated micro-organisms in turbulence”. In: *Journal of Fluid Mechanics* 739 (2014), pp. 22–36.

[34] Wikipedia. *Mixed layer — Wikipedia, The Free Encyclopedia*. [Online; accessed 15-November-2017]. 2017. URL: `https://en.wikipedia.org/w/index.php?title=Mixed_layer&oldid=805600756`.

[35] Clement de Boyer Montegut et al. "Mixed layer depth over the global ocean: An examination of profile data and a profile-based climatology". In: *Journal of Geophysical Research: Oceans* 109.C12 (2004).

[36] Keith E Brainerd and Michael C Gregg. "Surface mixed and mixing layer depths". In: *Deep Sea Research Part I: Oceanographic Research Papers* 42.9 (1995), pp. 1521–1543.

[37] Rafel Simó and Carlos Pedrós-Alió. "Role of vertical mixing in controlling the oceanic production of dimethyl sulphide". In: *Nature* 402.6760 (1999), pp. 396–399.

[38] Wikipedia. *Shearwater — Wikipedia, The Free Encyclopedia*. [Online; accessed 15-November-2017]. 2017. URL: `https://en.wikipedia.org/w/index.php?title=Shearwater&oldid=804206007`.

[39] Jacopo G Cecere et al. "Commercial fisheries, inter-colony competition and sea depth affect foraging location of breeding Scopoli's Shearwaters Calonectris diomedea". In: *Ibis* 157.2 (2015), pp. 284–298.

[40] Leandro Bugoni, Liliana D'Alba, and Robert W Furness. "Marine habitat use of wintering spectacled petrels Procellaria conspicillata, and overlap with longline fishery". In: *Marine Ecology Progress Series* 374 (2009), pp. 273–285.

[41] Michelle A Kappes et al. "Hawaiian albatrosses track interannual variability of marine habitats in the North Pacific". In: *Progress in Oceanography* 86.1 (2010), pp. 246–260.

[42] Iván Ramírez et al. "Year-round distribution and habitat preferences of the Bugio petrel". In: *Marine Ecology Progress Series* 476 (2013), pp. 269–284.

[43] Thomas A Clay et al. "Proximate drivers of spatial segregation in non-breeding albatrosses". In: *Scientific reports* 6 (2016).

[44] Daniel Oro et al. “Influence of food availability on demography and local population dynamics in a long-lived seabird”. In: *Proceedings of the Royal Society of London B: Biological Sciences* 271.1537 (2004), pp. 387–396.

[45] Robert JM Crawford and Bruce M Dyer. “Responses by four seabird species to a fluctuating availability of Cape Anchovy Engraulis capensis off South Africa”. In: *Ibis* 137.3 (1995), pp. 329–339.

[46] J Gasparini et al. “Food availability affects the maternal transfer of androgens and antibodies into eggs of a colonial seabird”. In: *Journal of evolutionary biology* 20.3 (2007), pp. 874–880.

[47] Matthew D Johnson and Thomas W Sherry. “Effects of food availability on the distribution of migratory warblers among habitats in Jamaica”. In: *Journal of Animal Ecology* 70.4 (2001), pp. 546–560.

[48] Atle Mysterud and Rolf Anker Ims. “Functional responses in habitat use: availability influences relative use in trade-off situations”. In: *Ecology* 79.4 (1998), pp. 1435–1441.

[49] Vers N Agostini and Andrew Bakun. “Ocean triads’ in the Mediterranean Sea: physical mechanisms potentially structuring reproductive habitat suitability (with example application to European anchovy, Engraulis encrasicolus)”. In: *Fisheries Oceanography* 11.3 (2002), pp. 129–142.

[50] Ewan D Wakefield, Richard A Phillips, and Jason Matthiopoulos. “Quantifying habitat use and preferences of pelagic seabirds using individual movement data: a review”. In: *Marine Ecology Progress Series* 391 (2009), pp. 165–182.

[51] EK Stenevik, S Sundby, and R Cloete. “Influence of buoyancy and vertical distribution of sardine Sardinops sagax eggs and larvae on their

transport in the northern Benguela ecosystem". In: *African Journal of Marine Science* 23 (2001), pp. 85–97.

[52] WK Koched et al. "Environmental conditions influencing the larval fish assemblage during summer in the Gulf of Gabes (Tunisia: South central Mediterranean)". In: *Mediterranean Marine Science* 16.3 (2015), pp. 666–681.

[53] Gabrielle A Nevitt, Richard R Veit, and Peter Kareiva. "Dimethyl sulphide as a foraging cue for Antarctic procellariiform seabirds". In: *Nature* 376.6542 (1995), pp. 680–682.

[54] Henri Weimerskirch. "Are seabirds foraging for unpredictable resources?" In: *Deep Sea Research Part II: Topical Studies in Oceanography* 54.3 (2007), pp. 211–223.

[55] Frederic Bartumeus et al. "Fishery discards impact on seabird movement patterns at regional scales". In: *Current Biology* 20.3 (2010), pp. 215–222.

[56] Ewan D Wakefield et al. "Space partitioning without territoriality in gannets". In: *Science* 341.6141 (2013), pp. 68–70.

[57] Jacopo G Cecere, Giorgia Gaibani, and Simona Imperio. "Effects of environmental variability and offspring growth on the movement ecology of breeding Scopoli's shearwater Calonectris diomedea". In: *Current Zoology* 60.5 (2014), pp. 622–630.

[58] Richard E Thomson and Isaac V Fine. "Estimating mixed layer depth from oceanic profile data". In: *Journal of Atmospheric and Oceanic Technology* 20.2 (2003), pp. 319–329.

[59] H Peters, MC Gregg, and JM Toole. "Meridional variability of turbulence through the equatorial undercurrent". In: *Journal of Geophysical Research: Oceans* 94.C12 (1989), pp. 18003–18009.

[60] Grigory Isayev and Levitus. *Seasonal variability of mixed layer depth for the world ocean*. US Department of Commerce, National Oceanic, Atmospheric Administration, National Environmental Satellite, Data, and Information Service, 1997.

[61] URL: `http://marine.copernicus.eu/` (visited on 10/13/2016).

[62] Nicholas Paul Fofonoff and RC Millard Jr. "Algorithms for the computation of fundamental properties of seawater." In: (1983).

[63] Intergovernmental Oceanographic Commission et al. "The International thermodynamic equation of seawater–2010: calculation and use of thermodynamic properties.[includes corrections up to 31st October 2015]." In: (2010).

[64] Joan Garriga et al. "Expectation-maximization binary clustering for behavioural annotation". In: *PloS one* 11.3 (2016), e0151984.

[65] Maite Louzao et al. "Coupling instantaneous energy-budget models and behavioural mode analysis to estimate optimal foraging strategy: an example with wandering albatrosses". In: *Movement ecology* 2.1 (2014), p. 8.

[66] URL: `http://www.bodc.ac.uk/projects/international/gebco/` (visited on 10/13/2016).

[67] URL: `http://oceancolor.gsfc.nasa.gov/` (visited on 10/13/2016).

[68] URL: `http://www.science.oregonstate.edu/ocean.productivity/index.php` (visited on 10/13/2016).

[69] URL: `https://en.wikipedia.org/wiki/Generalized_linear_mixed_model` (visited on 10/13/2016).

[70] Maurizio Sarà. "Feeding habits of Cory's shearwater (Calonectris diomedea) in the central Mediterranean Sea". In: *Status and conservation of*

seabirds. SEO/BirdLife and Medmaravis, Madrid (1993), pp. 213–220.

[71] José Manuel Arcos and Daniel Oro. "Significance of fisheries discards for a threatened Mediterranean seabird, the Balearic shearwater Puffinus mauretanicus". In: *Marine Ecology Progress Series* 239 (2002), pp. 209–220.

[72] Kenneth Henry Mann and John RN Lazier. *Dynamics of marine ecosystems: biological-physical interactions in the oceans*. John Wiley & Sons, 2013.

[73] Marianna Giannoulaki et al. "The spatial distribution of anchovy and sardine in the northern Aegean Sea in relation to hydrographic regimes". In: *Belgian Journal of Zoology* 135.2 (2005), p. 151.

[74] Isabel Afán et al. "Foraging movements and habitat niche of two closely related seabirds breeding in sympatry". In: *Marine biology* 161.3 (2014), pp. 657–668.

[75] David Grémillet et al. "A junk-food hypothesis for gannets feeding on fishery waste". In: *Proceedings of the Royal Society of London B: Biological Sciences* 275.1639 (2008), pp. 1149–1156.

[76] Jacopo G Cecere et al. "Movement patterns and habitat use during incubation and chick-rearing of Cory's shearwaters (Calonectris diomedea diomedea)(Aves: Vertebrata) from Central Mediterranean: influence of seascape and breeding stage". In: *Ital. J. Zool. (Modena)* 80.1 (2013), pp. 82–89.

[77] JOSÉ P GRANADEIRO et al. "Flexible foraging strategy of Cory's shearwater, Calonectris diomedea, during the chick-rearing period". In: *Animal Behaviour* 56.5 (1998), pp. 1169–1176.

[78] MC Magalhães, RS Santos, and KC Hamer. "Dual-foraging of Cory's shearwaters in the Azores: feeding locations, behaviour at sea and implications for food provisioning of chicks". In: *Marine Ecology Progress Series* 359 (2008), pp. 283–293.

[79] Manuel Barange and Ian Hampton. "Spatial structure of co-occurring anchovy and sardine populations from acoustic data: implications for survey design". In: *Fisheries Oceanography* 6.2 (1997), pp. 94–108.

[80] Teresa Militão et al. "Individual migratory patterns of two threatened seabirds revealed using stable isotope and geolocation analyses". In: *Diversity and Distributions* 19.3 (2013), pp. 317–329.

[81] Frederick Schram et al. *Treatise on Zoology-Anatomy, Taxonomy, Biology. The Crustacea, Volume 9 Part A: Eucarida: Euphausiacea, Amphionidacea, and Decapoda (partim)*. Vol. 9. BRILL, 2010.

[82] Vitor H Paiva et al. "Foraging plasticity in a pelagic seabird species along a marine productivity gradient". In: *Marine Ecology Progress Series* 398 (2010), pp. 259–274.

[83] G.M. Viswanathan et al. *The Physics of Foraging: An Introduction to Random Searches and Biological Encounters*. Cambridge University Press, 2011. ISBN: 9781139497558.

[84] Pierre Bovet and Simon Benhamou. "Spatial analysis of animals' movements using a correlated random walk model". In: *Journal of theoretical biology* 131.4 (1988), pp. 419–433.

[85] Gandhimohan M Viswanathan et al. "Lévy flight search patterns of wandering albatrosses". In: *Nature* 381.6581 (1996), p. 413.

[86] GM Viswanathan et al. "Optimizing the success of random searches". In: *Nature* 401.6756 (1999), 911–914. ISSN: 0028-0836.

[87] Monique de Jager et al. “Lévy walks evolve through interaction between movement and environmental complexity”. In: *Science* 332.6037 (2011), pp. 1551–1553.

[88] Enrica Pollonara et al. “Olfaction and topography, but not magnetic cues, control navigation in a pelagic seabird: displacements with shearwaters in the Mediterranean Sea”. In: *Sci. Rep.* 5 (2015).

[89] Andrew M Reynolds et al. “Pelagic seabird flight patterns are consistent with a reliance on olfactory maps for oceanic navigation”. In: *Proc. R. Soc. B* (2015).

[90] WS Lewellen and RI Sykes. “Analysis of concentration fluctuations from lidar observations of atmospheric plumes”. In: *Journal of climate and applied meteorology* 25.8 (1986), pp. 1145–1154.

[91] Erik Sparre Andersen. “On sums of symmetrically dependent random variables”. In: *Scandinavian Actuarial Journal* 1953.sup1 (1953), pp. 123–138.

[92] Antonio Celani, Emmanuel Villermaux, and Massimo Vergassola. “Odor landscapes in turbulent environments”. In: *Phys. Rev. X* 4.4 (2014), p. 041015.

[93] Wade R McGillis et al. “Carbon dioxide flux techniques performed during GasEx-98”. In: *Marine Chemistry* 75.4 (2001), pp. 267–280.

[94] NOAA. `http://coastwatch.pfeg.noaa.gov/erddap/info/jplCcmpL3Wind6Hourly_LonPM180/index.html`. Online; last access: Thu, 09 Jun 2016 10:12:42 GMT. 2016.

[95] Scott Chamberlan. *rerddap: General Purpose Client for ERDDAP Servers.* `https://github.com/ropensci/rerddap`. R package version 0.3.4. 2016.

[96] R Core Team. *R: A Language and Environment for Statistical Computing*. R Foundation for Statistical Computing. Vienna, Austria, 2015. URL: `https://www.R-project.org/`.

[97] Andrew M. Edwards et al. "Revisiting Levy flight search patterns of wandering albatrosses, bumblebees and deer". In: *Nature* 449.7165 (2007), 1044–U5.

[98] Anna Gagliardo et al. "Oceanic navigation in Cory's shearwaters: evidence for a crucial role of olfactory cues for homing after displacement". In: *J. Exp. Biol.* 216.15 (2013), 2798–2805.

[99] O Padget et al. "Anosmia impairs homing orientation but not foraging behaviour in free-ranging shearwaters". In: *Sci. Rep.* 7 (2017).

[100] Gustav Kramer. "Experiments on bird orientation and their interpretation." In: *Ibis* 99.2 (1957), pp. 196–227. ISSN: 1474-919X.

[101] Hans G Wallraff. *Avian navigation: pigeon homing as a paradigm*. Springer Science & Business Media, 2005.

[102] Stefano Focardi and Jacopo G. Cecere. "The Levy flight foraging hypothesis in a pelagic seabird". In: *J. Anim. Ecol.* 83.2 (2014), pp. 353–364. ISSN: 1365-2656.

[103] Vitor H Paiva et al. "Flight dynamics of Cory's shearwater foraging in a coastal environment". In: *Zoology* 113.1 (2010), pp. 47–56.

[104] Andrei V Komolkin et al. "Theoretically possible spatial accuracy of geomagnetic maps used by migrating animals". In: *J. R. Soc. Interface* 14.128 (2017), p. 20161002.

[105] Martin Wikelski et al. "True navigation in migrating gulls requires intact olfactory nerves". In: *Sci. Rep.* 5 (2015). ISSN: 2045-2322.

[106] Cornelia Buehlmann et al. "Desert ants use olfactory scenes for navigation". In: *Anim. Behav.* 106 (2015), pp. 99 –105.

[107] Jennifer L DeBose and Gabrielle A Nevitt. “The use of odors at different spatial scales: comparing birds with fish”. In: *J. Chem. Ecol.* 34.7 (2008), pp. 867–881.

[108] COMSOL Inc.. 2017. URL: `https://www.comsol.it/`.

[109] F. Hecht. “New development in FreeFem++”. In: *J. Numer. Math.* 20.3-4 (2012), pp. 251–265. ISSN: 1570-2820.

[110] Colin K Drummond and Frederic A Lyman. “Mass transfer from a sphere in an oscillating flow with zero mean velocity”. In: *Computational Mechanics* 6.4 (1990), pp. 315–326.

[111] George B Jeffery. “The motion of ellipsoidal particles immersed in a viscous fluid”. In: 102.715 (1922), pp. 161–179.

[112] Laurent Chevillard and Charles Meneveau. “Lagrangian dynamics and statistical geometric structure of turbulence”. In: *Physical review letters* 97.17 (2006), p. 174501.

[113] Andrei D Polyanin et al. *Hydrodynamics, mass and heat transfer in chemical engineering*. Vol. 14. CRC Press, 2001.

[114] John Happel and Howard Brenner. *Low Reynolds number hydrodynamics: with special applications to particulate media*. Vol. 1. Springer Science & Business Media, 2012.

[115] Markus Nyberg, Tobias Ambjörnsson, and Ludvig Lizana. “A simple method to calculate first-passage time densities with arbitrary initial conditions”. In: *New Journal of Physics* 18.6 (2016), p. 063019.